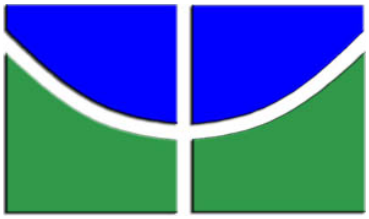

University of Brasilia

Physics Institute

Masters Dissertation

Aggregation Effects on Energy Transfer between Chloroaluminum Phthalocyanine and Graphene Oxide

Fernando Teixeira Bueno

Advisor: Prof. Pedro Henrique de Oliveira Neto

Co-Advisor: Dr. Leonardo Evaristo de Sousa

Aggregation Effects on Energy Transfer between Chloroaluminum Phthalocyanine and Graphene Oxide

Written by

Fernando Teixeira Bueno

Dissertation presented to the Physics Institute at the University of Brasilia for the obtention of the masters degree.

Physics Institute - University of Brasilia.

Brasilia. May, 2022.

"Not only is the Universe stranger than we think, it is stranger than we can think."

Werner K. Heisenberg

Acknowledgments

First and foremost I thank my family, specially my parents, Roberto and Anamaria, my sister, Gabriela and my grandmother, Lucia, for the unconditional support during all my life and in the pursuit of an academic career. I thank my high school Physics teacher, Paula Menezes for first introducing me to the world of Physics. I am immensely grateful to Professor Dr. Pedro Henrique for all the partnership, friendship and incentive for the last five years. Also, I thank my co-advisor Dr. Leonardo Evaristo for numerous valuable contributions in my formation. I thank my colleagues from the research group, Larissa Born e Laura Simonassi for walking down this path with me and supporting each other in reaching our academic goals. Furthermore, I thank my lifelong friends Laura Kuser, Thais Pacheco, Kauê Venzi, Michella de Castro and Isabel Perez for all the friendship and support over the last decade; you were vital for me to get this far. Also, I thank the friends I met over the last 2 years during the pandemic, Charlotte, Patrick, Austin, Sarah and Page, who made two very challenging years full of joy. I would like to pay my respects to late Professor Jorge Fernandes Barroso and thank him for the honor of having been his student; I carry you very fondly in my memory. Furthermore, I thank my late grandparents Marietta and Roberto Bueno, whom I wish could be here to participate in this moment, I'm hoping I can make them proud. Lastly, I thank Professor Leonardo Paterno, from the Institute of Chemistry at the University of Brasilia for his invaluable support and kindness in providing experimental data that was paramount in the development of this work.

Abstract

Cancer is currently one the most devastating diseases requiring aggressive treatments. The search for alternative treatment options led to the use of Photodynamic Therapy (PDT) and Photothermal Therapy (PTT). PDT works upon the combination of photosensitizing agents with specific wavelength light exposure in order to produce reactive oxygen species (ROS), inducing cellular oxidative stress and/or apoptosis. In this context, the photosensitizing agent stands out in PDT due to its capacity of producing ROS and the multiple successes it has had with the use of multiple transport platforms. Meanwhile, PTT is based on the combination of photothermal agents that increase the temperature by means of light absorption. Graphene oxide (GO) has been used in PTT due to its absorption capability, resulting in high temperature increase, which leads to effective tumor ablation. The combination of both treatments can be promising, leading to synergistic effects. Indeed, such combinations have been experimentally investigated, however leading to the observation of quenching effects in the emission signal of the PDT agent. Thus, possibly compromising the effectiveness of the PDT treatment. In this work, we simulated exciton dynamics in AlClPc and GO, through the process of Förster Resonance Energy Transfer using a combination of density functional theory and a Kinetic Monte Carlo method. Analysis shows the Förster mechanism as a competing factor in regards to the photoluminescence of the phthalocyanine. Our results with the use of the KMC algorithm allowed for the determination of an approximate Förster radius for an $AlClPc-GO$ heterodimer based on a molecular aggregation. Such method exemplifies a top-down approach where one can extract electronic structure results from molecular dynamics simulations.

CONTENTS

LIST OF FIGURES

CHAPTER 1

OVERVIEW

Cancer is one of the deadliest diseases in modern day [1]. State of the art research is of paramount importance when it comes to finding alternative treatments. Among the current most effective courses of treatment are chemotherapy, radiotherapy and surgical removal. The one thing they have in common is their perniciousness to the patient, leading to several debilitating temporary or permanent side effects. The quest for less encroaching protocols lead to the discovery of photodynamic (PDT) and photothermal therapies (PTT). The former is based on the electronic excitation of photosensitizing agents, which typically are biocompatibilized dyes — such as methylene blue and different phthalocyanines — to generate oxidative stress on several types of cancerous cells [2, 3, 4, 5]. The latter utilizes photosensitive agents — to which there are numerous possibilities of materials and protocols — to generate local heat and induce thermal ablation. Graphene based materials have been extensively explored for these

applications in nanomedicine because of their low cost, large molecular surface area, chemical and mechanical stability, low toxicity, and biocompatibility. Also, graphene based systems, may exhibit high photonic energy absorption in the near infrared radiation (NIR) range, making it a prominent candidate for PTT [6, 7, 8].

The human body has several tools to induce cellular damage or apoptosis, one of which happens through producing reactive oxygen species (ROS). In a biological context, ROS are a natural product from oxygen's metabolization and play an essential role in maintaining homeostasis. Nevertheless, high levels of ROS do not necessarily translate to an individual being healthy or cancer free [9]. Photodynamic therapy is an up-and-coming less invasive form of cancer treatment. The principals behind it are simple: a photosensitizing agent is inserted in the affected area and exposed to light within a certain wavelength that promotes maximum photon absorption. The dye will then emit photons which will, in turn, induce photodynamic biochemical reactions that may produce ROS in that specific region. With that in mind, one can infer that PDT is, in theory, a very precise and safe way to eliminate cancer. However, its efficacy is intrinsically connected to the agent's molecular structure. Most widely used agents have a heterocyclic structure of aromatic rings similar to chlorophyll or globin — protein present in our blood — the majority of which were discovered in the late 1980's or 1990's. Nowadays, photodynamic agents are categorized into three large families: (i) porphyrin based compounds (figure 1.1(a)); (ii) chlorophyll based molecules (figure 1.1(b)) ; (iii) dye based (figure 1.1(c) [10]. The latest generation of explored photosensitizing molecules is mostly made of metallic phthalocyanines, whose typical structure is shown in figure 1.1(c).

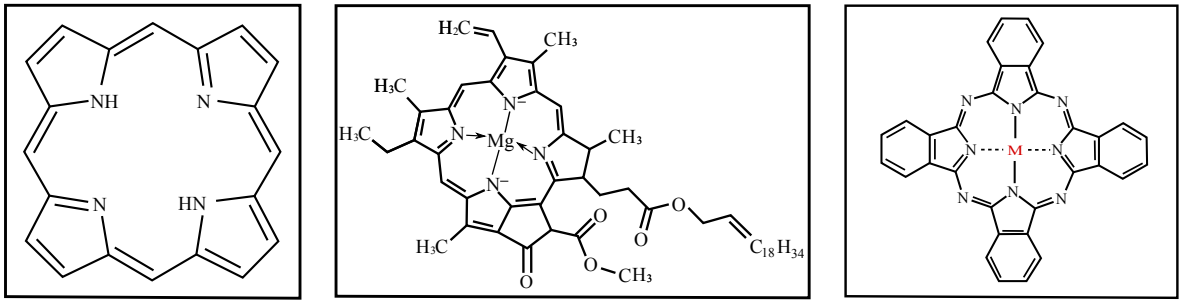

(a) (b) (c)

Figure 1.1: a) Porphyrin's structural formula. b) Typical structural formula for chlorophyll based compounds. c) General structural formula for metallic phthalocyanines where the central atom is presented in red, labeled as *M*.

Concurrently to advancements in PDT, photothermal therapy has also gained significant ground in the medical field when it comes to cancer treatments. Similar to PDT, PTT requires an intermediary agent that, when injected into the patient, affects a specific region after being exposed to adequate light. Nevertheless, there is no ROS production being induced. The protocol relies on heat generation and temperature elevation, requiring appropriate absorption in order for the compound to be excited and to undergo non-radiative relaxation. Such relaxation prompts an increase in kinetic energy, therefore causing the local temperature to increase. Elevated temperatures tend to cause cellular damage, whether it happens through the rupture of the membrane or some sort of protein imbalance. Among the more relevant compounds used in PTT, we can list gold nanoparticles — due to their high absorption capacity in NIR — dye-based nanoparticles, carbon nanotubes and graphene oxide nanoparticles — due to its high biological compatibility, low toxicity and high capacity to convert light into heat [11].

Analyzing both forms of treatments, it's reasonable to expect that combining said therapies might yield more efficient treatments with simultaneous ROS production and temperature increase. Experimental studies have indeed identified a synergistic effect between both therapies

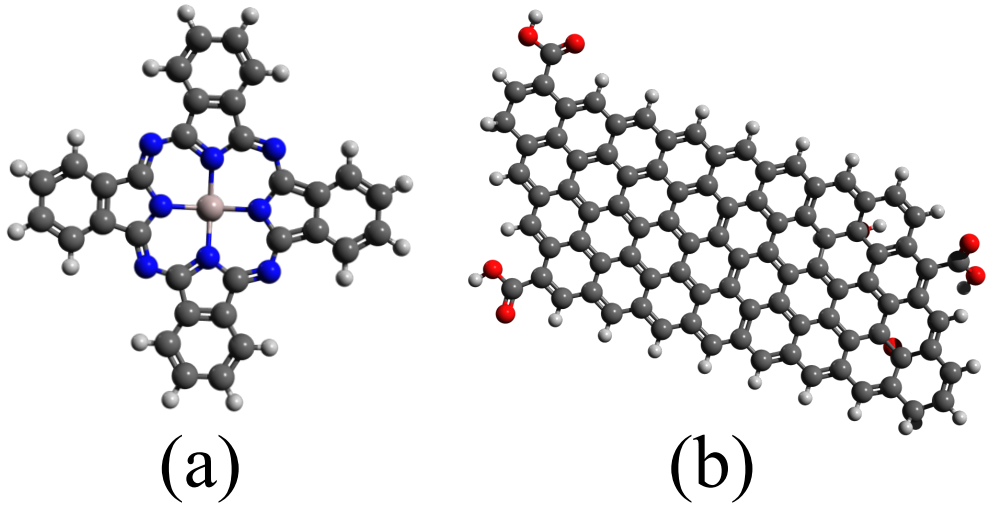

Figure 1.2: a) Chloroaluminum phthalocyanine schematic representation. A aluminum-chlorine bond perpendicular to the molecule's plane is not displayed due to going inwards the paper. b) Schematic representation of graphene oxide.

when simultaneously executed [12, 13], with methylene blue and graphene oxide acting as photodynamic and phototermal agents, respectively. Notwithstanding, several spectroscopic measurements were performed over the interaction between chloroaluminum phthalocyanine (AlClPc) and -graphene oxide (nGO) [14]. The authors' investigation led to the observation of quenching in emission spectra from the resulting structure (AlClPc + nGO). Furthermore, ROS suppression was discovered when different graphene oxide species were inserted into the solution. It is worth mentioning that the dye's photoluminescence process and ROS generations, although correlated, are independent phenomena. With that in mind, these results suggest the combination of the aforementioned agents may not be effective, due to observed quenching.

Objectives

In this present work, we investigate chloroaluminum phthalocyanine's electronic structure (figure 1.2(a)) and its interaction with nano-graphene oxide (nGO — figure 1.2(b)). As a center object of investigation hereby presented, the cause for experimentally observed quenching was not clear. We create an interaction model based on the energy transfer between dye molecules and from *AlClPc* to graphene oxide. Initially, electronic structure calculations were performed for the phthalocyanine at different levels via Density Functional Theory (DFT) and its time-dependent extension (TD-DFT). Experimental data was supplied by Professor Leonardo Paterno from the Chemistry Institute at the University of Brasilia (UnB). From said data, we were able to create a morphology that could be simulated using a Kinetic Monte Carlo (KMC) algorithm. At this point it is worth noting that the calculated morphological parameters challenged the KMC model previously employed by the Atomic and Molecular Physics group from the Institute of Physics at the University of Brasilia, forcing us to implement several new corrections in order to circumvent such problems. These corrections are explained in detail in chapters 2 and 3.

Our hypothesis focuses on the occurrence of molecular aggregation between *AlClPc* molecules surrounding nGO sheets, which decreases intermolecular distances and enhances energy transfer. The unknown value of the energy transfer rate between *AlClPc* and *nGO* became a parameter in our simulations due to the computational difficulty in obtaining it. We aim to ascertain missing electronic structure parameters from molecular dynamics results in a top-down approach. The experimental data is used as a mirror to what our results should aim to reproduce.

This dissertation is split in eight chapters: in chapter 2, a general but thorough review of the underlying physical models that describe the investigated processes is presented. In chapter 3, the methodology for each step of the process is presented as well as a detailed description of the system's morphology and how the employed KMC model was constructed. In chapter 4 we present the experimental data kindly provided by Professor Paterno followed by our results from electronic structure calculations and KMC simulations. Chapter 5 summarizes the work and highlights the main conclusions. Chapters 6, 7 and 8 are appendices with additional information on chapters 2, 3 and 4, where we also present results that were omitted from chapter 4 in order to keep the text objective and concise.

CHAPTER 2

PHYSICAL BACKGROUND

2.1 Density Functional Theory

In the fundamental basis of solving the many-body problem in a molecular context, lies the Hartree-Fock method. At its core is the use of the variational method considering that the wave function can be represented by a single Slater determinant. Nevertheless, dealing with the wave function is not a simple task. The idea of working with a more suitable quantity instead of the wave function itself gave way to massive developments in computational quantum mechanics and chemistry. The mathematical basis that will be used in this section is detailed in Appendix B, where we demonstrate that the energy of a system can be written as a functional

of the electron density,

$$E[\rho] = T[\rho] + V_{ee}[\rho] + V_{ne}[\rho] \tag{2.1}$$

$$= T[\rho] + V_{ee}[\rho] + \int d\vec{r}\vartheta(\vec{r})\rho(\vec{r}) \tag{2.2}$$

in which, $T[\rho]$, $V_{ee}[\rho]$ and $V_{ne}[\rho]$ represent the kinetic energy, the electron-electron interaction and the nucleus-electron functionals, respectively and

$$\vartheta(\vec{r}) = \sum_{i}^{N}\sum_{A}^{M}\frac{Z_A}{r_{iA}}.$$

In density functional theory (DTF), the idea is to determine a functional, namely $S[\rho]$, employing the variational method with associated restriction to the electron density, ρ, which will have the form of

$$S[\rho] = \left(\int d\vec{r}(\hat{O}_1 + \hat{O}_2)\right)\rho(\vec{r}) - \mu\left(\int d\vec{r}\rho(\vec{r}) - N\right). \tag{2.3}$$

The practical problem is that $\hat{O}_1$ and $\hat{O}_2$ are not exactly found. Next we are going to enunciate and demonstrate the two Hohenberg-Kohn theorems that serve as the basis for DFT.

Hohenberg-Kohn Theorems

In DFT terms, electrons interact with each other through an external potential determined by the nuclei. Here, we show that once such potential is known, the ground state electron density can be determined and, by extension, so can the system's minimum energy.

Theorem 1: for a test function $\bar{\rho}(\vec{r})$ that satisfies $\int d\vec{r}\bar{\rho}(\vec{r}) = N$, being N the number of electrons, and $\bar{\rho}(\vec{r}) \geq 0$ we have that $E[\bar{\rho}(\vec{r})] > E[\rho(\vec{r})]$, where ρ is the exact solution.

The proof is very simple and it is done within the variational method, where it's shown that with

$$E[\bar{\rho}(\vec{r})] = \langle \bar{\psi} | \hat{H} | \bar{\psi} \rangle \qquad\qquad E[\rho(\vec{r})] = \langle \psi | \hat{H} | \psi \rangle \tag{2.4}$$

then, once the variational principle assures that $\langle \bar{\psi} | \hat{H} | \bar{\psi} \rangle \geq \langle \psi | \hat{H} | \psi \rangle$, necessarily, $E[\bar{\rho}(\vec{r})] \geq E[\rho(\vec{r})]$, being the equal sign valid only when $\bar{\rho}(\vec{r}) = \rho(\vec{r})$ the exact electronic density.

Theorem 2: the ground state electron density is uniquely determined by the external potential $\vartheta(\vec{r})$.

This demonstration will be done via *reductio ad absurdum*, where we show that an assumption contrary to this theorem yields an impossible result. For that, consider two different external potentials, ϑ_A and ϑ_B, that define two corresponding wave functions, ψ_A and ψ_B, that in turn, define densities ρ_A and ρ_B. From the variational method, we have that

$$\langle \psi_A | H_A | \psi_A \rangle < \langle \psi_B | H_A | \psi_B \rangle \tag{2.5}$$

where the left-hand side is

$$\langle \psi_A | H_A | \psi_A \rangle = \langle \psi_A | T | \psi_A \rangle + \langle \psi_A | V_{ee} | \psi_A \rangle + \int d\vec{r}\vartheta_A \rho_A. \tag{2.6}$$

Comparing equation (2.6) to equation (7.2), we can see that — for the same number of electrons,

$N_A = N_B$ — the first and last terms in (7.2) are identical in systems A and B, i.e. $T_A = T_B = T$ and $V_{eeA} = V_{eeB}$. While the remaining term in (7.2) differs in A and B due to a parametric dependence on the position of the nuclei. The right-hand side in (2.6) is

$$\langle \psi_B | H_A | \psi_B \rangle = \langle \psi_B | T | \psi_B \rangle + \langle \psi_B | V_{ee} | \psi_B \rangle + \int d\vec{r} \vartheta_A \rho_B \tag{2.7}$$

leading equation (2.6) to become

$$\langle \psi_A | T | \psi_A \rangle + \langle \psi_A | V_{ee} | \psi_A \rangle + \int d\vec{r} \vartheta_A \rho_A < \langle \psi_B | T | \psi_B \rangle + \langle \psi_B | V_{ee} | \psi_B \rangle + \int d\vec{r} \vartheta_A \rho_B \tag{2.8}$$

Let us take the hypothesis where $\rho_A = \rho_B$, then equation (2.8) is reduced to

$$\langle \psi_A | T | \psi_A \rangle + \langle \psi_A | V_{ee} | \psi_A \rangle < \langle \psi_B | T | \psi_B \rangle + \langle \psi_B | V_{ee} | \psi_B \rangle . \tag{2.9}$$

Now, taking H_B and applying the same procedure we have,

$$\langle \psi_A | H_B | \psi_A \rangle > \langle \psi_B | H_B | \psi_B \rangle , \tag{2.10}$$

then

$$bra\psi_A T | \psi_A \rangle + \langle \psi_A | V_{ee} | \psi_A \rangle > \langle \psi_B | T | \psi_B \rangle + \langle \psi_B | V_{ee} | \psi_B \rangle . \tag{2.11}$$

Finally, comparing equations (2.9) and (2.11) we have a mathematically absurd result. Hence, the hypothesis of two different external potentials resulting in equivalent densities is denied.

We know how to write the kinetic energy operator, $\hat{T}$, and the electron-electron interaction operator, $\hat{V}_{ee}$. However, we do not know how to express them as a functional of ρ, all we known is that it is possible. It is worth noting that both operators depend on the number of electrons, N, such that is reasonable to assume that for different systems with the same N, they will have the same form. In practical terms, each system is individualized only by the electron-nucleus interaction, namely $\vartheta(\vec{r})$. The fact that we don't know how to express them as functionals individually allows for us to define $F_{HK} = T[\rho] + V_{ee}[\rho]$, which is known as Hohenberg-Kohn's universal functional. Thus, the energy in the DFT approximation can be determined as

$$E[\rho] = F_{HK}[\rho] + \int d\vec{r}\vartheta(\vec{r})\rho(\vec{r}). \tag{2.12}$$

The next step, analog to what is done in the Hartree-Fock method, is to determine the functional that minimizes the energy above. There is no explicit exact form for the functional F_{HK}. Nevertheless, the functional we want to obtain can be expressed as

$$S[\rho] = F_{HK}[\rho] + \int d\vec{r}\vartheta(\vec{r})\rho(\vec{r}) - \mu\left(\int d\vec{r}\rho(\vec{r}) - N\right) \tag{2.13}$$

where μ is a Lagrange multiplier. It is important to write this functional in terms of integrals in order to facilitate minimization through the method shown in Appendix B. Moreover, equation

(2.13) can be translated to

$$S[\rho] = \int d\vec{r}\rho(\vec{r})df_{HK} + \int d\vec{r}\vartheta(\vec{r})\rho(\vec{r}) - \mu\int d\vec{r}\rho(\vec{r}) + \mu N \tag{2.14}$$

$$= \int d\vec{r}\left(df_{HK} + \vartheta(\vec{r}) - \mu\right)\rho(\vec{r}) + \mu N \tag{2.15}$$

which can be compared to equation (7.45) to visualize that $\mathscr{L} = \rho(\vec{r})(df_{HK} + \vartheta(\vec{r}) - \mu)$.

Proceeding to minimize $S[\rho]$, we make $\rho(\vec{r}) \to \rho(\vec{r}) + \varepsilon(\vec{r})$ such that

$$d\mathscr{L} = \varepsilon(\vec{r})df_{HK} + \varepsilon(\vec{r})\vartheta(\vec{r}) - \varepsilon(\vec{r})\mu \tag{2.16}$$

$$= \varepsilon(\vec{r})\left(df_{HK} + \vartheta(\vec{r}) - \mu\right) \tag{2.17}$$

leading to

$$dS = \int d\vec{r}\varepsilon(\vec{r})\left(df_{HK} + \vartheta(\vec{r}) - \mu\right) = 0 \Longrightarrow df_{HK} + \vartheta(\vec{r}) = \mu. \tag{2.18}$$

Although it is an important result, equation (2.18) is vague. We are looking for the density that minimizes the energy and satisfies equation (2.18), but determining $F_{HK}[\rho]$ is still a challenge.

Kohn-Sham Method

The previously demonstrated theorems emphasize how the electron density determines the external potential, which then determines the Hamiltonian, which in turn, determines the wave function. However, if this algorithm is used, its final step is still to solve Schrödinger's equation for that Hamiltonian, which can be unimaginably difficult. When we refer to molecular

orbitals, the difficulty in solving such system comes from the interactions between electrons, computed in $F_{HK}[\rho]$ within the Hamiltonian. In 1965, Kohn and Sham thought of a simplification of the problem by completely disregarding the electron-electron interactions. As a result, the Kohn-Sham Hamiltonian could be written simply as a sum of one-electron operators. It would have Slater determinants as eigenfunctions composed of each individual electron eigenfunctions and their eigenvalues are the sum of one-electron eigenvalues.

The Hamiltonian of an arbitrary system (we shall call it the $\mathscr{A}$ system) where electrons do not interact will be, as said before, a sum of one-electron operators,

$$H^{\mathscr{A}} = \hat{T}_{\mathscr{A}} + \hat{V}_{\mathscr{A}} \tag{2.19}$$

$$= \sum_{i}^{N} \left(-\frac{1}{2}\nabla_i^2 + \vartheta(\vec{r}_i) \right) \tag{2.20}$$

$$= \sum_{i}^{N} h^{\mathscr{A}}(\vec{r}_i) \tag{2.21}$$

where the individual one-electron Hamiltonians $h^{\mathscr{A}}$ solutions are spin orbitals (χ_i) that satisfy $h^{\mathscr{A}}(\vec{r}_i)\chi_i(\vec{x}_i) = \mathscr{E}_i\chi_i(\vec{x}_i)$. Those solutions can be combined into a Slater determinant to form the solution to $H^{\mathscr{A}}$. Naming the solution to $H^{\mathscr{A}}$ as Λ, we have

$$\Lambda(\vec{x}_1,\vec{x}_2,...,\vec{x}_N) = \frac{1}{\sqrt{N!}} \sum_{i}^{N!} (-1)^{\mathscr{P}_i} \mathscr{P}_i(\chi_1\chi_2...\chi_N) \tag{2.22}$$

which satisfies $H^{\mathscr{A}}\Lambda(\vec{x}_1,\vec{x}_2,...,\vec{x}_N) = E_{\mathscr{A}}\Lambda(\vec{x}_1,\vec{x}_2,...,\vec{x}_N)$, where $E_{\mathscr{A}}$ is the energy.

The kinetic energy and electron-nucleus interactions functionals for the $\mathscr{A}$ system are

$$T_{\mathscr{A}}[\rho] = \langle \Lambda | \hat{T}_{\mathscr{A}} | \Lambda \rangle \tag{2.23}$$

$$= \sum_{i}^{N} \langle \chi_i | \left(-\frac{1}{2}\nabla^2 \right) | \chi_i \rangle \tag{2.24}$$

and

$$V_{\mathscr{A}}[\rho] = \langle \Lambda | \hat{V}_{\mathscr{A}} | \Lambda \rangle \tag{2.25}$$

$$= \sum_{i}^{N} \langle \chi_i | \vartheta(\vec{r}_i) | \chi_i \rangle . \tag{2.26}$$

Therefore, the energy is simply,

$$E_{\mathscr{A}}[\rho] = T_{\mathscr{A}}[\rho] + \int d\vec{r} \rho(\vec{r}) \vartheta(\vec{r}) \tag{2.27}$$

leading to

$$S_{\mathscr{A}}[\rho] = E_{\mathscr{A}}[\rho] - \mu \left(\int d\vec{r} \rho(\vec{r}) - N \right) \tag{2.28}$$

Here we can proceed with the exact same steps done before where we turn $T_{\mathscr{A}}[\rho] = \int d\vec{r} d\tau_{\mathscr{A}}$, find $d\mathscr{L} = d\tau_{\mathscr{A}} + \vartheta(\vec{r}) - \mu$ to minimize $S_{\mathscr{A}}[\rho]$, yielding

$$\mu = d\tau_{\mathscr{A}} + \vartheta(\vec{r}). \tag{2.29}$$

Kohn and Sham's brilliance was to apply the results obtained for the $\mathscr{A}$ system to an actual molecular system. We reproduce their work below.

Kohn-Sham for a Molecular System

It is known that the missing correlation energy between anti-parallel spin orbitals in Hartree-Fock is an important flaw in their results for most molecular systems. Making an *ad-hoc* correction for such correlation in equation (7.43) we obtain the Kohn-Sham energy,

$$E_{KS}[\rho] = T[\rho] + V_{ne}[\rho] + \mathscr{J}[\rho] - \mathscr{K}[\rho] + E_{xc}[\rho] \tag{2.30}$$

$$= T[\rho] + \int d\vec{r}\rho(\vec{r})\vartheta(\vec{r}) + \mathscr{J}[\rho] - \mathscr{K}[\rho] + E_{xc}[\rho] \tag{2.31}$$

$$= T[\rho] + \int d\vec{r}\rho(\vec{r})\vartheta(\vec{r}) + V_{ee}^{KS}[\rho] \tag{2.32}$$

in which we can add $0 = T_{\mathscr{A}}[\rho] - T_{\mathscr{A}}[\rho] + \mathscr{J}[\rho] - \mathscr{J}[\rho]$ to rearrange it as,

$$E_{KS}[\rho] = T_{\mathscr{A}}[\rho] + \mathscr{J}[\rho] + (V_{ee}^{KS}[\rho] + T[\rho] - T_{\mathscr{A}}[\rho] - \mathscr{J}[\rho]) + \int d\vec{r}\rho(\vec{r})\vartheta(\vec{r}) \tag{2.33}$$

where the terms in parenthesis determine the *exchange and correlation functional*, $E_{XC}[\rho]$, leading to

$$E_{KS}[\rho] = T_{\mathscr{A}}[\rho] + \mathscr{J}[\rho] + E_{XC}[\rho] + \int d\vec{r}\rho(\vec{r})\vartheta(\vec{r}) \tag{2.34}$$

To nobody's surprise, once we have the energy of Kohn-Sham as a functional of the

electron density, the next step is to minimize it. Defining

$$S_{KS}[\rho] = E_{KS}[\rho] - \mu\left(\int d\vec{r}\rho(\vec{r})\vartheta(\vec{r}) - N\right) \tag{2.35}$$

$$= \int d\vec{r}\rho(\vec{r})\left(d\tau_{\mathscr{A}} + dj + de_{xc} + \vartheta(\vec{r}) - \mu\right) + \mu N \tag{2.36}$$

$$= \int d\vec{r}\mathscr{L}_{KS} + \mu N \tag{2.37}$$

from where we can obtain,

$$dS_{KS}[\rho] = 0 = \int d\vec{r} d\mathscr{L}_{KS} \tag{2.38}$$

in which,

$$d\mathscr{L}_{KS} = \varepsilon(\vec{r})d\tau_{\mathscr{A}} + dj_{int} + \varepsilon(\vec{r})de_{xc} + \varepsilon(\vec{r})\vartheta(\vec{r}) - \mu. \tag{2.39}$$

The term dj_{int} corresponds to the integral from of $\int d\vec{r}\rho(\vec{r})dj$, which is the only one we have yet to define. In order to do that, we need to take $\mathscr{J}[\rho]$ in terms of $\rho(\vec{r})$ as defined in equation (7.43) so that we can proceed as,

$$\int d\vec{r}\rho(\vec{r})dj = \frac{1}{2}\int d\vec{r}\rho(\vec{r})\int d\vec{r}'\rho(\vec{r}')\frac{1}{|\vec{r}-\vec{r}'|} \tag{2.40}$$

and with $\rho(\vec{r}) \to \rho(\vec{r}) + \varepsilon(\vec{r})$,

$$d j_{int} = \frac{1}{2} \int d\vec{r} \varepsilon(\vec{r}) \int d\vec{r}' \rho(\vec{r}') \frac{1}{|\vec{r} - \vec{r}'|} + \int d\vec{r} \rho(\vec{r}) \int d\vec{r}' \varepsilon(\vec{r}') \frac{1}{|\vec{r} - \vec{r}'|} \tag{2.41}$$

$$\tag{2.42}$$

where we can exchange $\vec{r} \to \vec{r}'$ and $\vec{r}' \to \vec{r}$, to write

$$d j_{int} = \int d\vec{r} \varepsilon(\vec{r}) \int d\vec{r}' \rho(\vec{r}') \frac{1}{|\vec{r} - \vec{r}'|} \tag{2.43}$$

$$\tag{2.44}$$

Placing this result in equation (2.39), we have

$$d\mathscr{L}_{KS} = \varepsilon(\vec{r}) \left(d\tau_{\mathscr{A}} + \int d\vec{r}' \rho(\vec{r}') \frac{1}{|\vec{r} - \vec{r}'|} + de_{xc} + \vartheta(\vec{r}) - \mu \right) \tag{2.45}$$

yielding

$$\mu = d\tau_{\mathscr{A}} + \int d\vec{r}' \rho(\vec{r}') \frac{1}{|\vec{r} - \vec{r}'|} + de_{xc} + \vartheta(\vec{r}) \tag{2.46}$$

$$= d\tau_{\mathscr{A}} + V_{eff}(\vec{r}) \tag{2.47}$$

defining an effective potential as,

$$V_{eff}(\vec{r}) = \vartheta(\vec{r}) + de_{xc} + \int d\vec{r}' \rho(\vec{r}') \frac{1}{|\vec{r} - \vec{r}'|}. \tag{2.48}$$

Equation (2.47) can be compared to equation (2.29), which we know how to solve and has

$$\rho(\vec{r}) = \sum_{i}^{N_\alpha} |\psi_i^\alpha|^2 + \sum_{i}^{N_\beta} |\psi_i^\beta|^2 \tag{2.49}$$

as its density, in which ψ_i is the i-th spatial orbital and α and β represent the corresponding electron spin.

The development performed above was based on the $\mathscr{A}$ system where we neglected every electron-electron interaction. There is a more straight forward development to obtain the Kohn-Sham equations without the comparison to system $\mathscr{A}$. It is available in Appendix B.

To summarize, Kohn-Sham equations are

$$h_{KS}\psi_i(\vec{r}) = \left(-\frac{1}{2}\nabla^2 + V_{eff}(\vec{r})\right)\psi_i(\vec{r}) = \varepsilon_k \psi_i(\vec{r}) \tag{2.50}$$

$$V_{eff}(\vec{r}) = \vartheta(\vec{r}) + \int \frac{\rho(\vec{r}')}{|\vec{r} - \vec{r}'|} + \vartheta_{XC}(\vec{r}) \tag{2.51}$$

$$\rho(\vec{r}) = \sum_{i} |\psi_i(\vec{r})|^2. \tag{2.52}$$

It is important to emphasize a key difference between Hartree-Fock and Density Functional Theory. DFT itself is derived without any approximation, and, in principle, it is an exact method. However, one would need to know E_{XC} as a functional of ρ in order to solve a molecular system exactly. Even though Hohenberg-Kohn theorems guarantee the existence of a density dependent functional, they do not provide the means to find it. Hartree-Fock, on the other hand, is deliberately an approximation where we consider a single Slater determinant as sufficient

solution to the electronic problem. The approximate part in DFT takes place in trying to obtain E_{XC}, whose exact form is unknown.

Kohn-Sham Self-Consistent Field

In practical terms of using DFT in computational packages to actually calculating electronic structure data, we follow a self consistent field methodology. First we expand Kohn-Sham orbitals in a basis set, namely $\{\phi_\theta\}$ and insert it in equation (2.50) to obtain

$$\psi_i(\vec{r}) = \sum_\theta c_{\theta i}\phi_\theta(\vec{r}) \Rightarrow h_{KS}\sum_\theta c_{\theta i}\phi_\theta(\vec{r}) = \varepsilon_i \sum_\beta c_{\theta i}\phi_\theta(\vec{r}) \tag{2.53}$$

which we can multiply by ϕ_η^* and integrate over the space to get

$$\sum_\theta \int d\vec{r}\phi_\eta^* h_{KS} c_{\theta i}\phi_\theta = \varepsilon_i \sum_\theta \int d\vec{r} c_{\theta i}\phi_\eta^*\phi_\theta = \varepsilon_i \sum_\theta S_{\eta\theta} c_{\theta i} \tag{2.54}$$

where $S_{\eta\theta}$ is the overlap between ϕ_η^* and ϕ_θ. This equation can be written as a matrix problem, as such

$$\mathbf{h}_{KS}\mathbf{C} = \varepsilon\mathbf{S}\mathbf{C} \tag{2.55}$$

As seen above, V_{eff} depends on the wave function and, consequently, depends on the chosen basis $\{\phi\}$. With a selected basis set, we create an attemptive ρ which determines V_{eff}. Then, we solve equation (2.55) and determine the expansion coefficients. If the coefficients converge to the initial guessed ones, then the problem is solved. If not, the process is repeated with the new set of coefficients. This algorithm is displayed in figure 2.1.

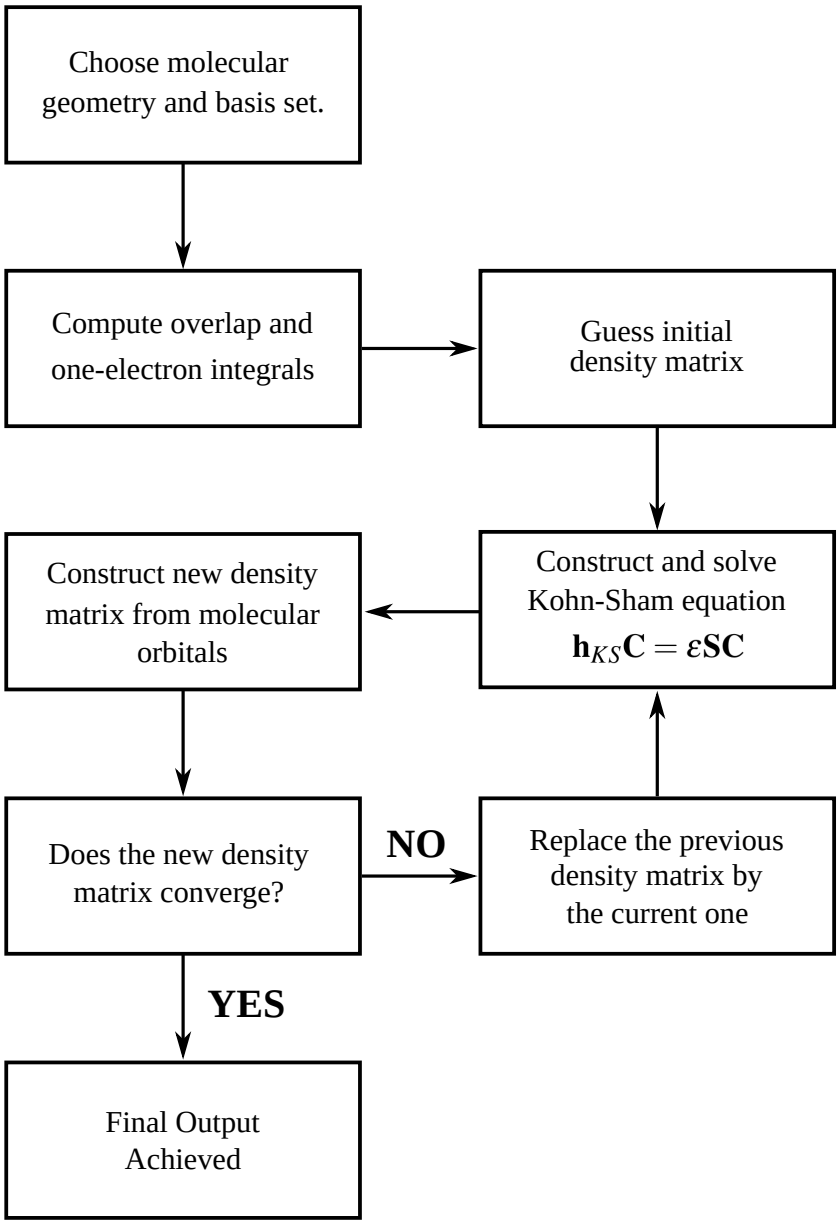

Figure 2.1: Self-consistent field methodology for Kohn-Sham equations in Density Functional Theory.

2.2 Nuclear Ensemble Method

The use of UV-vis spectroscopy is of paramount importance to the general characterization of materials [15, 16]. Obtaining absorption and emission spectra is essential because they

determine, in a first approximation, the best application for a certain material. There are several approaches and computational packages to simulate these types of spectra [17, 18, 19]. In the Franck-Condon (FC) method, the transition probability is proportional to the square of wave function overlap integral [20, 21]. The approximation is limited to cases where the optimized geometries are not significantly different in the molecule's ground and excited state. However, such difference is generally non-negligible for organic molecules, where there is a loss of energy to the lattice due to relaxation effects. Thus, FC method has been shown inaccurate for flexible organic molecules [22].

Recently, simulation methods based on electronic excitation have gained ground due to their computational feasibility and reasonably accurate results [23, 24]. More specifically, methods that consist on the excitation of an ensemble of geometrical conformations around the optimized geometry for a certain electronic state. The formal derivation of the equations that surround this method leads to finding the absorption cross section and the differential emission rate. Such procedure makes use of time-dependent perturbation theory, considers the interaction between an electron and a classical external field in the context of the Born-Oppenheimer approximation [25].

The nuclear ensemble method makes use of the normal mode frequencies obtained from optimized geometries in an electronic state. A transformation into the configuration space is made in such way that the molecule is approximated by a set of independent harmonic oscillators whose frequencies equal the molecule's normal mode frequencies. The ensemble

is generated through the use of the following distribution,

$$\rho(\vec{r},T) = \prod_{i=1}^{3N-6} \left(\frac{\mu_i \omega_i}{2\pi\hbar \sinh(\hbar\omega_i/k_B T)} \right)^{1/2} \exp\left(-\frac{\mu_i \omega_i}{\hbar} r_i^2 \tanh\left(\frac{\hbar\omega_i}{2k_B T} \right) \right) \tag{2.56}$$

where $\vec{r}$ is the normal coordinate, T is the temperature, k_B is Boltzmann's constant, μ_i and ω_i are the i-th state's reduced mass and normal mode frequency, respectively. It is important to notice that this distribution is not normalized.

A sample of several geometries (N_g) act as input to single point TD-DFT calculations that return vertical transition energies ΔE. The spectrum is found through the convolution of Gaussian curves G with a standard deviation δ and calculated vertical transition energies as their mean value gathered from each conformation,

$$\sigma(E) = \frac{\pi e^2 \hbar}{2mc\varepsilon_0} \frac{1}{N_g} \sum_i^{N_g} f_i G(E - \Delta E_i, \delta) \tag{2.57}$$

where c is the speed of light, e is the electron's charge, m is its mass, ε_0 is the vacuum permittivity and f_i is the oscillator strength. The latter is related to the transition dipole moments μ by

$$f_i = \frac{2m\Delta E_i \mu_i^2}{3\hbar^2 e^2}. \tag{2.58}$$

For the emission spectra, first excited state (S_1) calculations are used. The results are averaged and lead to the differential emission rate, defined by

$$\phi(E) = \frac{e^2}{2\pi\hbar mc^3\varepsilon_0} \frac{1}{N_g} \sum_i^{N_g} \Delta E_i^2 f_i G(E - \Delta E_i, \delta) \tag{2.59}$$

2.3 Förster Resonance Energy Transfer

Excitons are neutral quasiparticles that carry energy throughout a molecular system. Energy transfer in organic systems is mainly described by Förster Resonance Energy Transfer (FRET). This mechanism happens non-radiatively and is incoherent, which means the excitation is localized and transferred from molecule to molecule. Such process generally occurs in systems where molecules are distanced by tens of angstroms, depending on the compounds in question. Considering a donor-acceptor (D/A) pair, transfer takes place in such way that the donor returns from its first excited state to its ground state. The acceptor, in turn, absorbs the excitation and goes from its ground state to its first excited state, as shown in figure 2.2's schematic representation.

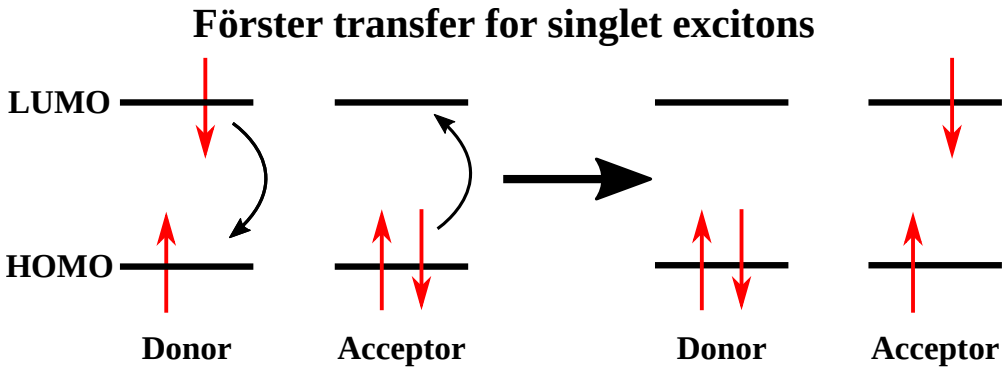

Figure 2.2: FRET mechanisms for singlet excitons.

By looking at the representation shown in figure 2.2, we can identify two states. First, to the left, in which the donor is excited (D^1) and the acceptor is not (A) which we can name $|D^1A\rangle$. Second, to the right, shows the donor back to its ground state (D) and the acceptor is now in its first excited state (A^1), namely $|DA^1\rangle$. If said state is stable enough in the system where it's located, this superposition state is known as *exciton* [26].

This particular form of exciton differs from others due to the fact that that both electron and hole remain in the same molecule. The electron and hole are located at the LUMO (Lowest Unoccupied Molecular Orbital) and HOMO (Highest Occupied Molecular Orbital), respectively. Such exciton is common in molecular crystals of aromatic compounds and in different classes of dyes, like the one investigated in this work.

The rate for which FRET takes place is given by [27]

$$k_F(r) = \frac{9c^4\kappa^2}{8\pi r^6}\int_0^\infty \frac{d\omega}{\omega^4}\phi_D(\omega)\sigma_A(\omega), \tag{2.60}$$

where c is the speed of light, κ is the orientation factor, r is the intermolecular distance (also know as the average hopping distance), $\phi_D(\omega)$ is the donor's differential emission rate and $\sigma_A(\omega)$ is the donor's absorption cross section. We utilize $\kappa^2 = 2/3$, resulting from considering the molecule to be an amorphous compound [28]. The rate decreases with the inverse of the typical D/A distance to the sixth power. The recombination (or emission) rate may be estimated by

$$k_{emi} = \frac{1}{\tau_{emi}} = \int_0^\infty \phi_D(\omega)d\omega \tag{2.61}$$

where τ_{emi} is the exciton's radiative lifetime.

The distance for which spontaneous recombination and hopping by FRET are equally probable is known the Förster radius. An expression for it can be obtained by $k_{emi} = k_F$,

$$R_F^6 = \frac{9c^4\kappa^2\tau_{emi}}{8\pi}\int_0^\infty \frac{d\omega}{\omega^4}\phi_D(\omega)\sigma_A(\omega). \tag{2.62}$$

We can also represent k_F in terms of the Förster radius,

$$k_F = \frac{1}{\tau_{emi}} \left(\frac{R_F}{\bar{r}} \right)^6 \tag{2.63}$$

Studies show that equation (2.63) overestimates the Förster rate for short distances, even if the definition of what a *short* distance means is unclear [29]. A correction for such problem takes the transition dipole moment μ into consideration to adjust the denominator in equation (2.63),

$$k_F = \frac{1}{\tau_{emi}} \left(\frac{R_F}{\gamma\mu + \bar{r}} \right)^6 \tag{2.64}$$

where $\gamma = 1.15\ e^{-1}$. Such correction defines an effective intermolecular distance [30, 31, 32].

It is important to mention that there is a minimum distance necessary for which FRET is dominant compared to other energy transfer mechanisms. As a necessary condition, the overlap between donor and acceptor orbitals has to be negligible. If that condition is not met, Dexter mechanisms prevails. Studies show that the minimum distance that meets those requirements is at least 5 Å. [33]

By studying the Förster mechanism in specific compounds, we can estimate certain efficiency indicators, such as the exciton diffusion length [34, 35, 36]. It is defined as the average distance which singlet excitons can diffuse before recombination. As explained in [31], exciton diffusion can be treated as a Wiener process and for such, experimental results show that it can be characterized as a normal diffusion [35, 37, 38, 39]. Under these assumptions,

exciton diffusion length can be analytically estimated as

$$L_D = r\left(\frac{R_F}{\gamma\mu + r}\right)^3. \tag{2.65}$$

CHAPTER 3

MODELING AND METHODOLOGY

3.1 Electronic structure

All electronic structure-related calculations contemplated in this work were performed using Gaussian 16 [40]. Gaussian 16 employs DFT and its time dependent extension. Geometry optimizations and normal mode analyses were executed for chloroaluminum phthalocyanine's both ground (S_0) and first excited (S_1) states using different functionals and methods within DFT. First, we utilized B3LYP and wB97XD functionals with 6-31G(d,p) basis set to obtain optimized geometries, vertical transition energies, and normal mode frequencies in gas phase. From S_1 calculations, we obtained the electric transition dipole moment, used in (2.64). However, the system of interest had its experiment executed in an ethanol solution. Thus, we performed the same calculations for both functionals considering the existence of a solvent through the use of PCM. The dielectric constant used was ethanol's in Gaussian 16, $\varepsilon = 24.852$. In addition,

in the ground state geometry, we calculated the vertical transition energies for AlClPc's 10 first excited states to evaluate possible higher excited state transitions and comparison with known experimental results. Results can be seen in Chapter 4.

3.2 Single Molecule Spectroscopy

Using the nuclear ensemble method with electronic structure results as inputs, we were able to simulate absorption and emission spectra for all S_0 and S_1 calculations. We employed this method through an algorithm developed by the Molecular Physics group from UnB [25]. Each optimized geometry yielded an ensemble of 500 geometrical conformations respective to normal mode frequencies from the distribution shown in (2.56). In the ensemble, each input was a single point calculation using TD-DFT in order to obtain vertical transition energies and oscillator strength for that specific conformation. Those results can be compiled, thus providing absorption and fluorescence spectra for AlClPc for the aforementioned electronic structure methods. The standard deviation in the convoluted gaussian curves was $\delta = k_b T$, where the temperature was $T = 300$ K.

The spectra are essential to the calculation of different exciton transfer and emission rates. From the fluorescence spectrum, we obtained the radiative exciton lifetime, τ_{emi}. By calculating the spectral overlap between the absorption and emission spectra we can calculate the Förster radius for any hetero or homodimer pair.

3.3 Kinetic Monte Carlo

This section will present the Kinetic Monte Carlo (KMC) algorithm employed in all the simulations. There are different models of the algorithm that can be implemented to simulate exciton dynamics [41, 42]. Over the last few months, we have developed three different algorithims within the research group. Due to the particularly challenging system morphology, we are going to elaborate on only one of the developed models, based on the choice of hopping neighbor. In addition, we explain in detail how we modeled the AlClPc-nGO system of interest based on experimental data.

3.3.1 Neighbor dependent KMC algorithm

Singlet exciton diffusion is widely simulated by KMC in several different systems and applications [43, 44, 45, 46]. As presented in Chapter 2, exciton diffusion process is ruled by FRET, where we know the rates for which the exciton emits (2.61) or hops between first neighbors (2.63). For simplification, let us consider a two dimensional (2D) lattice, as shown in 3.1. The gray squares represent molecules to where excitons can go. We will refer to those as possible sites. In blue, we have two excitons of which where all the first immediate neighboring sites are labeled from 1 to 8. The white spaces between adjacent sites represent the average intermolecular distance, namely $\bar{r}$, which is an important parameter, shown in (2.63).

Being in a 2D model, we have 9 important rates to consider, one respective to emission and eight regarding hopping possibilities. Normally, with single exciton simulations in a single material, there is only one time scale, which means the exciton can only hop to one of the

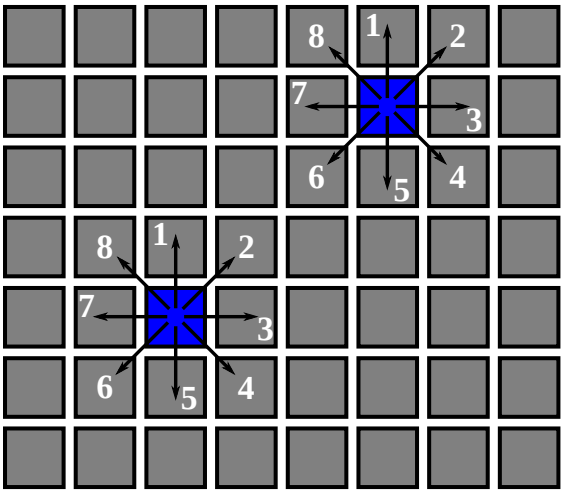

Figure 3.1: Example of a 2D lattice. Gray sites represent non-excited molecules and blue represent excitons in a localized molecule, leading it to its first excited state.

neighbors or it can be recombined. The rate according to which the exciton can emit is shown in (2.61) and displayed below,

$$k_{emi} = \frac{1}{\tau_{emi}}, \tag{3.1}$$

remembering that τ_{emi} is the exciton lifetime. When it comes to hopping to each of the neighbors, the Förster rate was defined in equation (2.64)

$$k_F = \frac{1}{\tau_{emi}} \left(\frac{R_F}{\gamma\mu + \bar{r}} \right)^6, \tag{3.2}$$

remembering that R_F is the Förster radius from the molecule in blue to any ith molecule labeled in 3.1. It is important to notice that for neighbors 1, 3, 5 and 7, the hopping rate is identical to (3.2). However, for neighbors 2, 4, 6 and 8, the excitons move a distance $\bar{r}$ in two dimensions, which leads to

$$k_F^{(2)} = k_F^{(4)} = k_F^{(6)} = k_F^{(8)} = \frac{1}{\tau_{emi}} \left(\frac{R_F}{\gamma\mu + \bar{r}\sqrt{2}} \right)^6 \tag{3.3}$$

in which $k_F^{(i)}$ is the hopping rate to the i-th neighbor. Naturally, extending this to three dimensions raises the number of neighbors from 8 to 26, where four of them are diagonal in three dimensions, which have $\gamma\mu + \bar{r}\sqrt{3}$ in the denominator of (3.2).

The probability of the i-th neighbor being chosen is calculated as

$$P_i = \frac{k_F^{(i)}}{\sum_j k_F^{(j)}} \tag{3.4}$$

and a random number is generated to make the selection. Notably, P_i does not depend on the emission rate. With the hopping site chosen, a second random number is generated to decide whether recombination or transfer takes place. The probability of exciton recombination is

$$P_{emi} = \frac{k_{emi}}{k_{emi} + k_F^{(i)}} = \frac{1}{1 + \left(\frac{R_F}{\gamma\mu + \bar{r}}\right)^6}. \tag{3.5}$$

Thus, the hopping probability can be expressed as

$$P_{hop} = 1 - P_{emi} = \frac{\left(\frac{R_F}{\gamma\mu + \bar{r}}\right)^6}{1 + \left(\frac{R_F}{\gamma\mu + \bar{r}}\right)^6}. \tag{3.6}$$

After each hopping takes place, the simulation clock advances from t to $t + dt$, where

$$dt = dt_{hop} = \frac{1}{k_F^{(i)}}. \tag{3.7}$$

By using this time step and keeping track of the times each exciton emits, ending the round in the simulation, we are able to compile time-resolved photoluminescence (TRPL) spectra. Such

spectra recover an exponential decay, respecting $exp(-t/\tau_{emi})$. However, for systems in which intermolecular distances are close to the material's Förster radius, excitons tend to fluoresce more than to hop. This happens due to the $\bar{r}^{-6}$ dependence in the denominator of (3.5), as previously mentioned. Figure 3.2 shows the comparison between TRPL obtained from two different systems and their respective corrections. In 3.2(a) we see a near perfect exponential fit where $R_F = 30$ Å, $\bar{r} = 10$ Å and $\tau_{emi} = 10$ ns. As for 3.2(c), the parameters were $R_F = 20$ Å with the same intermolecular distance and exciton lifetime. Notably, the fitting isn't accurate and the exponential behavior is not recovered.

Even in the case displayed in 3.2(a) being a perfect fit to the simulated data, exciton lifetime still presents an error of 1.6% compared to τ_{emi}. As for 3.2(c), the exponential function is fitted with a 5.7% fitting error, yielding a lifetime of 8.097 ns, meaning a 20% error compared to τ_{emi}.

With that in mind, we implemented a correction in the simulation's time step. In the case of an excessive number of early exciton recombination due to low probability of hopping, we implemented a third layer of decision once we had P_{emi} and P_{hop} calculated. The first correction is to have a known time step for each decision. If the exciton was selected to fluoresce, the corresponding time step was

$$dt_{emi} = \alpha \frac{1}{\frac{1}{\tau_{emi}} \left(\frac{R_F}{\gamma\mu + \bar{r}} \right)^6} \tag{3.8}$$

where α is an adjustable parameter greater than 0 until 1. In the case of hopping taking place, (3.7) is the respective time step. Lastly, we defined a parametric time step to improve the time

scale of events based on the hopping one. It is defined as

$$dt_{step} = \alpha dt_{hop}. \tag{3.9}$$

Once these quantities are defined, we calculated the probability of event occurrence, stipulated as

$$P_{occ} = \frac{dt_{step}}{dt} \tag{3.10}$$

where dt can be dt_{emi} for when the recombination is chosen and dt_{hop} in the case of hopping taking place. Then, a third random number is drawn to decide if the selected event actually occurs during that time step or if the first two decisions are retaken. In other words, P_{occ} is a way to ponder the occurrence of events in systems that have numerically challenging parameters. In addition, it represents a chance for the exciton to stand still during different time steps, where it doesn't get recombined, but it isn't necessarily transferred. Regarding to parameter α, it can change orders of magnitude depending on the system. In 3.2(b) we used $\alpha = 10^{-3}$ to improve simulated time scale, taking the fitted time from 9.84 ns to 10.03 ns, reducing the error by a factor of over four. Arguably, the system presented in 3.2(a) and 3.2(b) doesn't necessarily require such correction, due to the initial 1.6% difference being satisfactory. However, by looking at the case of $R_F = 20$ Å and applying the same correction, the fitted time is as good as the uncorrected one for $R_F = 30$ Å. Figure 3.2(d) shows the corrected TRPL for $R_F = 20$ Å.

It is essential to mention that this correction does not affect the actual diffusion process. It only improves the time scale of the simulation. This was verified by looking at the diffusion length with and without the implemented correction, which remains the same for both cases.

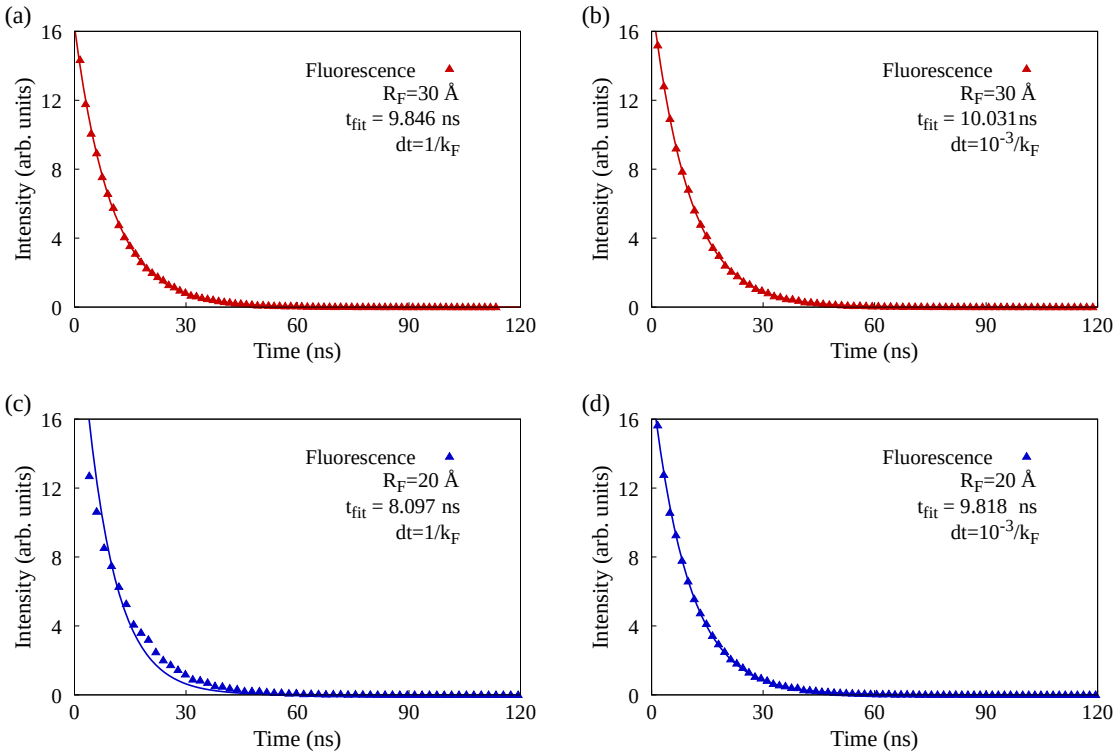

Figure 3.2: TRPL spectra for $R_F = 30$ Å while using $dt = 1/k_F$ (a) and $dt = 10^{-3}/k_F$ (b). TRPL spectra for $R_F = 20$ Å while using $dt = 1/k_F$ (c) and $dt = 10^{-3}/k_F$ (d).

In the following sections, we will discuss the correction used for the system of interest.

3.3.2 Modeling system morphology

Concerning the morphology, first we use the experimental concentrations of the compounds to calculate an approximate number of molecules in a certain volume. Using simple stoichiometry we calculated the number of AlClPc molecules in a volume of 1 L (10^{27} Å^3) for the concentrations shown in [14]. The dye has a molar mass of $M_{dye} = 574.96$ g/mol. For a given concentration of dye, ρ_{dye}, we have the number of AlClPc molecules, n_{ph},

$$n_{ph} = \frac{\rho_{dye} \cdot 6.02 \cdot 10^{23}}{M_{dye}} \tag{3.11}$$

As for the phototermal agent, we have to consider the fact that nGO is a two dimensional extended system with a multitude of possible sizes and masses, leading to an estimated mass corresponding to one 100 nm x 100 nm sheet of nGO based on the amount of carbon atoms present in one sheet. The proportion between oxygen and carbon atoms varies with the radicals present in each sample. Here, we account only for carbon atoms when calculating the mass.

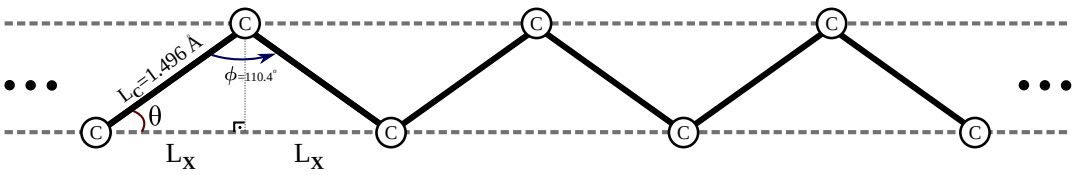

Figure 3.3: Graphene Oxide zig-zag edge.

In order to estimate the mass, we consider one sheet. Its extremities are visualized as shown in Figure 3.3, with the average carbon single bond length being 1.496 Å and an angle between two bonds connected to a carbon atom $\phi = 110.4^o$. Projecting it horizontally to a value of $L_x = 1.22$ Å, we can estimate the amount of carbon atoms on each side of a nGO sheet as

$$N_{C_{atoms}} \approx \frac{100\ nm}{L_x} = 819 \Longrightarrow N_C^T = 6.724 \times 10^5. \tag{3.12}$$

Given the dimensions of a nGO sheet, we can approximate the total amount of carbon atoms by $N^2_{C_{atoms}}$. Now, with a known atomic mass for carbon of $m_C = 12u$, considering $u = 1.66054 \times 10^{-24}$ g, we have the mass of a 100 nm x 100 nm sheet of $m_{nGO} = m_C u N^2_{C_{atoms}} = 1.339 \times 10^{-17}$ g. The next step is identical to the procedure applied to the dye, where we estimate the amount of

nGO sheets per concentration as

$$n_{nGO} = \frac{\rho_{nGO} \cdot 6.02 \cdot 10^{23}}{m_{nGO}}. \tag{3.13}$$

The results for quantifying the involved molecules are presented in table 3.1.

Compound	Exp. Concentration (g/L)	Number of Molecules
AlClPc	2.26	2.37×10^{21}
	0.31	3.25×10^{20}
nGO	2.96	2.21×10^{17}
	6.30	4.71×10^{17}
	12.65	9.47×10^{17}

Table 3.1: Number of molecules in a volume of 10^{27} Å^3

We want to simulate molecules of dye surrounded by nGO. For that we create a cubic lattice where the cube's faces represent the nGO sheets. In order to do that, and knowing the amount of molecules in our chosen volume of 10^{27} Å, we can calculate the proportion between dye and *nGO*. Since the cube has six *nGO* faces, we calculated said proportion as

$$P_{ph}^{(conc)} = \frac{n_{ph}}{6n_{nGO}^{(conc)}} \tag{3.14}$$

for the respective concentrations. We present the calculated proportions in table 3.2.

Now that we have the approximate number of molecules in our system, one of the most important parameters to be obtained is the approximate intermolecular distance, given its connection to the presented transfer rates. To obtain that, we consider the same arbitrary volume

ρ_{dye} (g/L)	ρ_{nGO} (g/L)	$P_{ph}^{(conc)}$
2.26	2.96	1784
	6.30	837
	12.65	416
0.31	2.96	244
	6.30	115
	12.65	57

Table 3.2: Amount of dye molecules interacting with nGO sheets according to experimental concentrations.

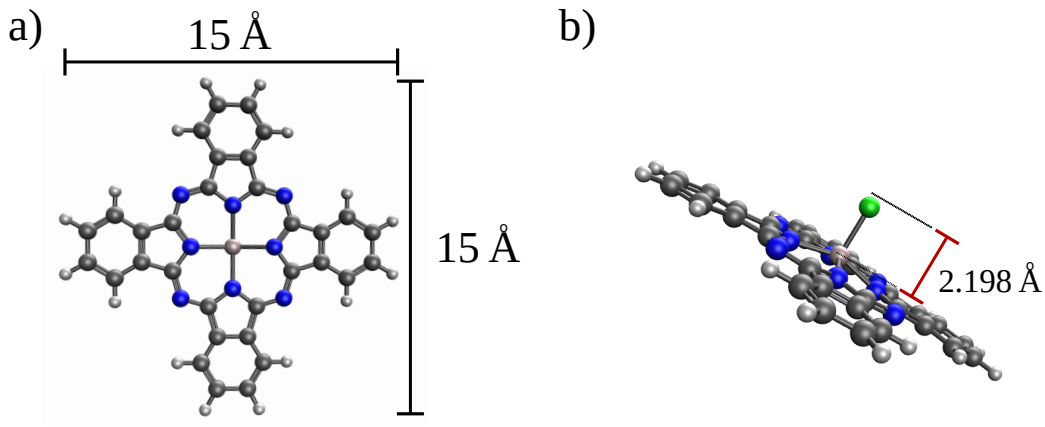

Figure 3.4: Aluminum Phthalocyanine Chloride dimensions. The perpendicular aluminum-chlorine bond inwards (a) and the molecule turned to the left displaying the perpendicular bond (b). Dark gray atoms represent carbon atoms, while light gray stands for hydrogen, blue for nitrogen and green for chlorine.

of 10^{27} Å^3 and calculate the "empty volume" (representing the solvent in the experiment) as

$$d = \sqrt[3]{\frac{10^{27} - n_{ph}V_{ph}}{n_{ph}}} \tag{3.15}$$

where V_{ph} is the volume of a phthalocyanine molecule in Å^3. Notice there are several ways we can calculate the dye's molecular volume. Considering the geometry shown in Figure 3.4, we have an extremely rigid molecule with only one atomic bond perpendicular to the molecule's plane. Therefore one approach we could take is to consider the molecule a small pyramid with a

15 Å x 15 Å square base and a height of 2.198 Å, which is the length for the aluminum-chlorine bond. This approach would yield a volume of 164.85 $Å^3$. A different option is to consider the molecule a block with two sides of 15 Å and a height equivalent to the Van der Waals radius for the carbon atom (1.7 Å), since the molecule is mostly composed by carbon. The yielded volume would be of 382.5 $Å^3$. Nonetheless, regardless of any reasonable approach we may prefer to calculate an individual molecule's volume, the $n_{ph}V_{ph}$ numerator in (3.16) will always be substantially inferior to 10^{27} $Å^3$, which simplifies our intermolecular distance to

$$d = \frac{10^9}{\sqrt[3]{n_{ph}}} \tag{3.16}$$

depending only on the concentration of dye. That said, we simulated systems for two different intermolecular distances, respective to the dye concentrations. For $\rho_{dye} = 2.26$ g/L we have $d_1 = 75$ Å , meanwhile for $\rho_{dye} = 0.31$ g/L we have $d_2 = 145$ Å.

Once all parameters are known, we assembled a cubic lattice, noting there was more than one approach to do so. The simpler approach is to consider the content of our cubic lattice of dye and use the intermolecular distance as a parameter to calculate the hopping rates from one randomly generated position to it's first 26 neighbors. Nevertheless, the size of our cubic lattice would need to be scanned to see which size length with a respective Förster radius yields satisfactory results when compared to experimental spectra. In an attempt to remove the guessing factor of the morphology and taking advantage of a known number of molecules and intermolecular distances, we were able to calculate how big the lattice would need to be in order to fit the estimated molecules for d_1 and d_2. Essentially, we are creating sites that excitons can

hop between before recombination. Excitons are randomly generated in any site, only being able to hop between the exact sites.

With a known intermolecular distance d_i $(i = 1,2)$, we can calculate the number of sites per lattice dimension as

$$N_{sites}^{(i)} = \sqrt[3]{P_{ph}^{(conc)} d_i} \tag{3.17}$$

related to a dimensional length $L_{(conc)}^{(i)}$ by

$$L_{(conc)}^{(i)} = N_{sites}^{(i)} d_i = {P_{ph}^{(conc)}}^{1/3} d_i^{4/3} \tag{3.18}$$

which we approximate to the closest integer (in angstroms). Our calculated parameters for the cubic lattice are presented in table 3.3.

ρ_{dye} (g/L)	ρ_{nGO} (g/L)	N_{sites}	$L_{(conc)}^{(i)}$ (nm)
2.26	2.96	52	383.6
	6.30	40	298.0
	12.65	32	236.1
0.31	2.96	33	476.0
	6.30	26	370.4
	12.65	20	293.1

Table 3.3: Lattice 1D length for each dye concentration and different nGO concentrations.

Notably, compared to typical systems where Förster transfer occurs [41, 46, 31], the intermolecular distances obtained through this morphology model are unusually large [47]. In chapter 4, we shall present all obtained results with the calculated distances. With this morphology, we weren't able to recreate the experimental data shown in section 4.1. For distances this big, because of the explicit dependence to r^{-6} on the Förster rate (2.63), it stands

to reason to assume that most excitons will have a higher likelihood of emitting instead of hopping in between dye molecules, as previously said.

There have been recent experimental studies on the formation of molecular aggregates in porphyrin based molecules with graphene oxide [48]. With that in mind, we created a simple aggregation model based on a geometric progression (GP).

Aggregation model

From the previous section, we have the basic system morphology. The size of the simulated box will remain the same. We simulated aggregation between dye molecules according to their distance from a nGO border. Since the box is very well defined and finite, we consider L_{box} as the sum S_n of the GP terms, defined by

$$S_n = A_1 \frac{(1-q^n)}{1-q} \tag{3.19}$$

where A_1 is the first term, q is the GP ratio and n is the number of sites, N_{sites}, defined in (3.18). Each known nGO concentration has its respective one-dimensional box length, which will serve as our boundary condition. With a known N_{sites} and a parametric ratio, we can simply rearrange (3.19) to obtain

$$A_1 = S_n \frac{(1-q)}{1-q^n} \tag{3.20}$$

from which we can calculate the n-th (n=1,2,3..) term as

$$A_n = A_{n-1} \cdot q = A_1 \cdot q^{n-1} \tag{3.21}$$

In order to better visualize the aggregation, figure 3.5(a) shows a 1D cross section of the box where all distances are the same, which means the terms of the GP are identical with a ratio $q = 1$. Whereas 3.5(b) shows the same section but with distances changing from the middle point of L_{box} towards the borders with $q < 1$. It is worth mentioning that we are considering the presence of nGO as the main cause for aggregation, so it's a natural consequence to consider the more central molecules to be the less affected by nGO presence.

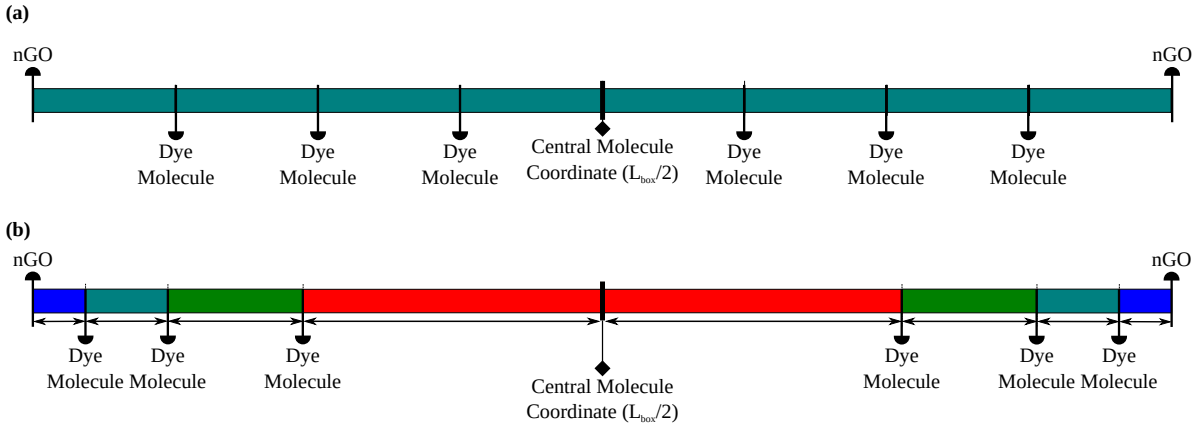

Figure 3.5: Equally distanced dye molecules, representing equally spaced sites in all directions (a). Different distances between dye molecules according to the present geometric progression (b).

We implemented the same progression in each dimension, allowing for a layer of dye to be aggregated to nGO vertically, but not necessarily horizontally or any other mutual combination between the three dimensions. Each coordinate corresponding to a dye molecule represents a possible site where excitons can be randomly generated. Note that the last coordinate on each side corresponds to a graphene-oxide "molecule", represented by the box's walls. This indicates the hopping to the far extremity on each side will be a Förster transfer between AlClPc as the donor molecule and nGO as the acceptor with our parametric Förster radius.

Considering the GP ratio as a parameter, table 3.4 shows the largest (represented

by the red bars in 3.5(a)) and the two smallest (displayed in a lighter blue and dark blue in 3.5(b)) distances for different ratios. Naturally, since the last coordinate in the progression corresponds to graphene-oxide, the smallest distance between dyes will be the second to last in each progression (mirrored in each side respective to a central molecule).

Calc. d_{dye} (Å)	q	A_1 (Å)	A_{n-1} (Å)	$d_{dye-nGO}$ (Å)
75	0.80	384.76	1.82	1.45
	0.84	310.21	4.73	3.96
	0.88	238.76	11.10	9.77
	0.90	205.04	16.35	14.72
	0.92	173.26	23.42	21.54
	0.94	143.87	32.58	30.63
	0.96	117.31	44.03	40.58
145	0.80	486.96	17.13	13.70
	0.84	401.52	34.96	24.67
	0.88	322.28	47.36	41.68
	0.90	285.63	58.81	52.92
	0.92	251.29	71.95	66.19
	0.94	219.45	86.75	81.54
	0.96	190.24	103.13	99.03

Table 3.4: Different values for first, second to last and last terms of the calculated geometric progression for the lowest nGO concentration (2.96 g/L) in each AlClPc concentration (2.26 g/L and 0.31 g/L - equivalent to distances $d_1 = 75$ Å and $d_2 = 145$ Å - with $L_{box} = 383.6$ nm and $L_{box} = 476.0$ nm, respectively) as shown in 3.3.

As displayed, due to it being a geometric progression, even a 20% aggregation increase on each site ($q = 0.8$) leads to extremely small distances between both dye molecules and from dye to nGO. Such distances carry no physical meaning, hence, our results will contemplate a maximum aggregation of 10% ($q = 0.90$) between dye molecules for the case where $\bar{r} = 75$ Å.

For better visualization of how the choice of ratio affects each distance between sites next to the central atom, as displayed in 3.5(b), figure 3.6 shows intermolecular distances for

four different chosen ratios considering the average non-aggregated distance of 75 Å. Figure 3.7 presents the same analysis for a average distance of 145 Å.

In figure 3.6(a) we see a maximum intermolecular distance of approximately 385 Å for $\rho_{nGO} = 2.96$ g/L and seven distances of over 100 Å when $q = 0.80$. Such high distances imply that excitons generated in the first 14 distances (7 to each side respective to the central molecule) would have a very small chance of being transferred. From (2.63) and (2.61) we have,

$$\frac{k_{emi}}{k_F} = \left(\frac{\bar{r}}{R_F}\right)^6 \approx \left(\frac{385}{91.7}\right)^6 \approx 5.5 \times 10^3, \tag{3.22}$$

representing an almost certain possibility of exciton recombination. As modeled, higher nGO concentrations translate into smaller simulated boxes or less possible sites where excitons can be generated. Since A_1 depends on the number of sites, as shown in (3.20), smaller boxes decrease the first term in the geometric progression. This can be seen in 3.6(b) and 3.6(c). However, for $q = 0.80$, in all cases, the smallest distances would have no physical value, even if a good range of sites are separated by distances under 100 Å .

The same description can be seen when we consider $\rho_{dye} = 0.31$ g/L, or 145 Å as average intermolecular distance. Looking at figure 3.7, we have the same ratios of aggregation leading to even higher distances for all different nGO concentrations. In this case, the number of sites are 17, 13 and 10 respective to $\rho_{nGO} = 2.26$ g/L, $\rho_{nGO} = 6.30$ g/L and $\rho_{nGO} = 12.65$ g/L. Obviously, the higher the number for q, the less aggregation is seen and the closer we get to the calculated average intermolecular distance. The simulated results obtained from implementing selected scenarios of aggregation with different morphologies can be seen in Chapter 4.

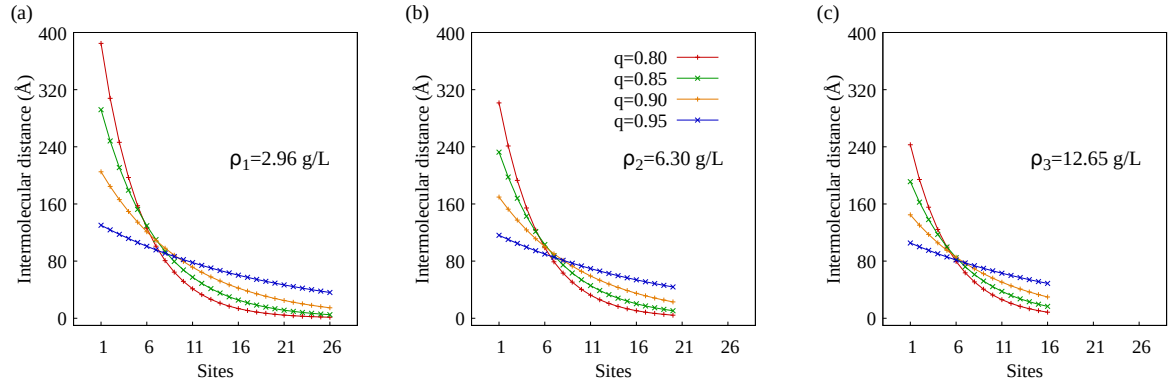

Figure 3.6: Intermolecular distances starting from the central molecule per number of sites considering different aggregation rates. Non-aggregate distance of 75 Å ($\rho_{dye} = 2.26$ g/L). In (a), there are 26 sites representing half of the sites in one dimension for a nGO concentration of 2.96 g/L. In (b) we have 20 sites for a concentration of 6.30 g/L, while in (c) we have it for 16 sites and 12.65 g/L, respectively.

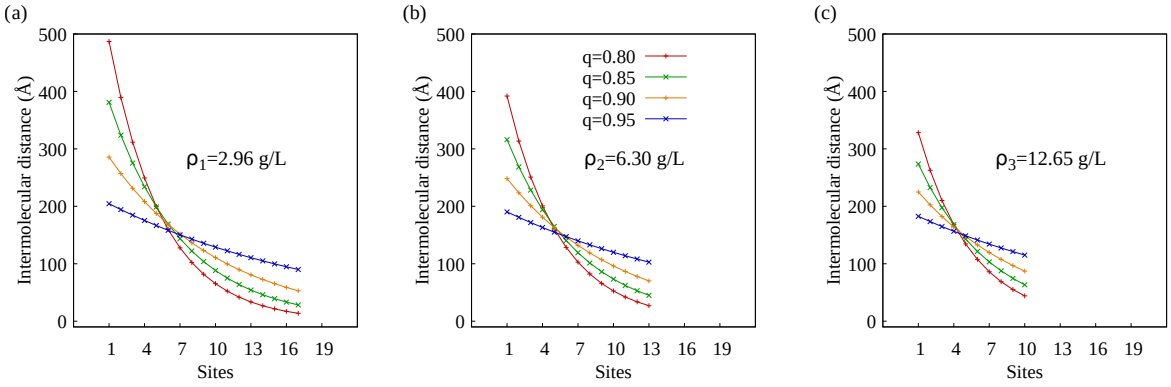

Figure 3.7: Intermolecular distances starting from the central molecule per number of sites considering different aggregation rates. Non-aggregate distance of 145 Å ($\rho_{dye} = 0.31$ g/L). In (a), there are 17 sites representing half of the sites in one dimension for a nGO concentration of 2.96 g/L. In (b) we have 13 sites for a concentration of 6.30 g/L, while in (c) we have it for 10 sites and 12.65 g/L, respectively.

All laid-out morphological parameters, such as intermolecular distances, number of sites and box length represent one dimensional amounts. In our simulations, we apply those parameters in every dimension. One can visualize our system morphology as a cubic box filled with differently spread out molecules of AlClPc with walls made of nGO that may collect excitons from dye molecules. Hence, the presence of nGO walls is expected to suppress dye fluorescence.

CHAPTER 4

RESULTS

4.1 Experimental study

All results displayed in this section were made available by Professor Leonardo Paterno from the Chemistry Institute at the University of Brasilia. The data shown below has already been published in his work "Quenching Effects of Graphene Oxides on the Fluorescence Emission and Reactive Oxygen Species Generation of Chloroaluminum Phthalocyanine", from 2018 on the Journal of Physical Chemistry A [14].

As said before, the reason for which the interaction between *AlClPc* and *nGO* caused such an expressive quenching in different configurations was not clear. The work consists of a spectroscopic investigation surrounding the aforementioned compounds. A few key results were used as guidelines to our investigation. In figure 4.1 we have the experimentally obtained absorption and emission spectra for *AlClPc* (a) and time-resolved photoluminescence spectra

for plain *AlClPc* and for a combination of it with different graphene oxide concentrations (b).

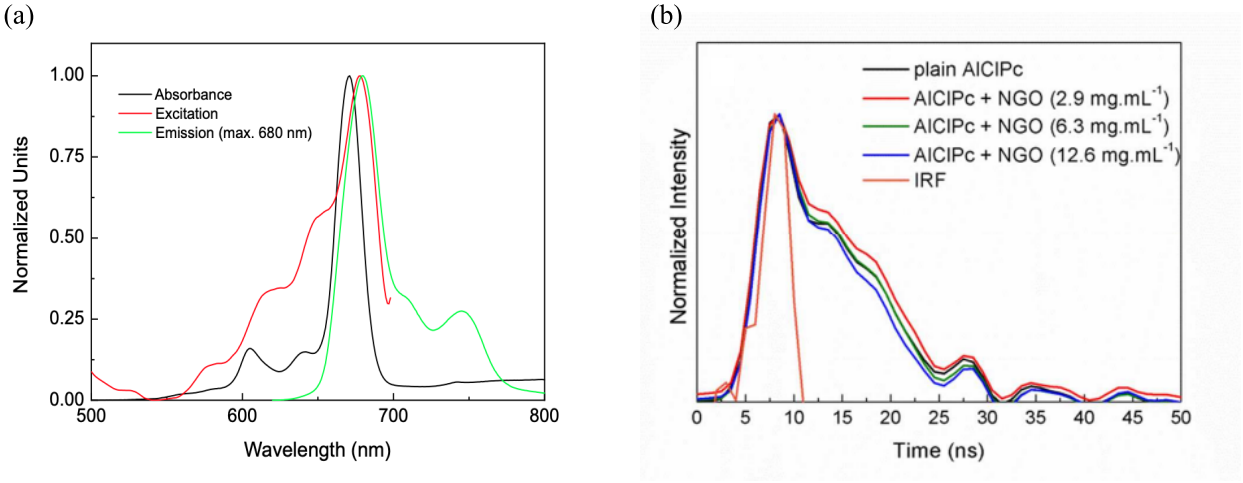

Figure 4.1: *AlClPc*'s experimentally obtained absorption and emission spectra (a) and TRPL spectra with and without different concentrations of graphene oxide (b).

Using a well established methodology (described in chapter 3), we simulated absorption and emission spectra and obtained TRPL information for plain dye simulations as well as for cases with different *nGO* concentrations. We shall present our computational results in the next section.

From looking at these results, we were able to list a number of hypothesis. Förster radius dependence on spectral overlap is known from equation (2.62), thus from figure 4.1a we can infer a high Förster radius between phthalocyanines. Absorption spectra has its peak at about 660 nm (1.87 eV), while emission spectrum peaks around 680 nm (1.82 eV). In addition, the near identical shape of the two spectra suggests little difference in electronic structure parameters between the dye's ground and first excited state. These assumptions were verified and are shown in the following sections. As for TRPL spectrum, we have limited resolution to properly fit exponential functions, from which we are able to interpret specific behaviors in the

energy transfer processes. The experimental authors obtained a fitted exciton radiative lifetime of approximately 7.5 ns.

Emission spectra were obtained in two different conditions: first, *nGO* and *AlClPc* were not in the same cuvette (spectra shown in figure 4.2a) - also leading to a considerable quenching; second measurements with the same experimental concentrations were made with the samples in the same cuvette (shown in figure 4.2b). All samples were in ethanol solutions.

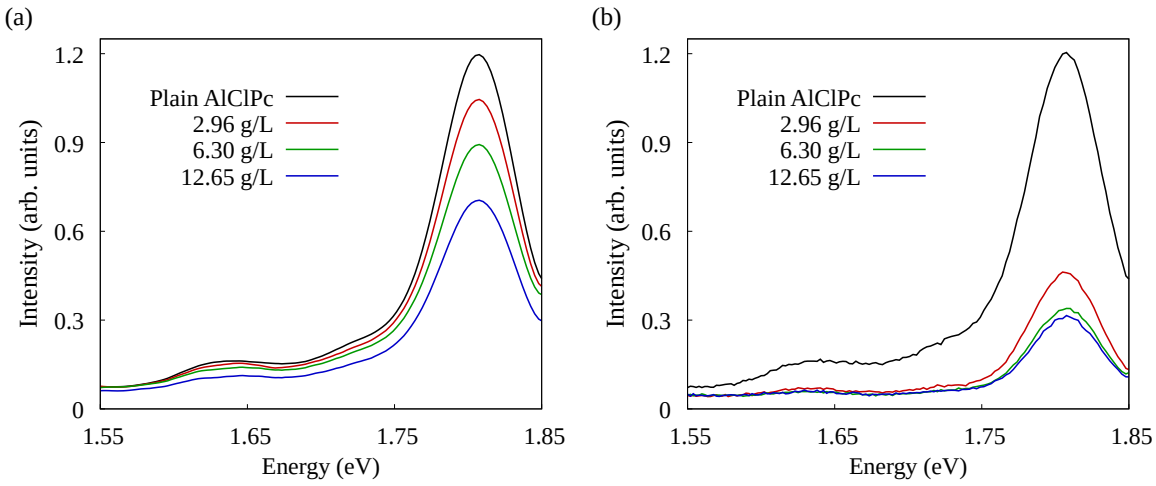

Figure 4.2: Experimentally obtained fluorescence spectra of AlClPc-nGO mixtures (a) in separated cuvettes and (b) in the same cuvette. *AlClPc* concentration in all mixtures: 0.31 g/L

Initially, quenching effect going from 15% to 50% (figure 4.2a) while the compounds are in different cuvettes may seem counter-intuitive. The physical barrier separating the samples prevents any and all form of energy transfer between them. Nevertheless, both samples are exposed to light simultaneously, leaving room for one solution to act as a filter to the other. Hence, we believe that the quenching is a direct result of less photons reaching the dye sample. The less light the dye absorbs, the less photons will it emit. The increase in *nGO* concentration translates to the filter being more intense, respectively reducing even more the amount of light

that reaches *AlClPc*.

When the spectra are measured in the same cuvette, the observed quenching is more expressive with nearly 60% emission quenching in the smallest *nGO* concentration. Quenching was calculated from the area beneath the spectra. Additionally, an increase in *nGO* concentration does not enhance quenching phenomena as intensively as it did in separate cuvettes. We mapped out the observed quenching per *nGO* concentration, which is displayed in table 4.1. Such intense reduction in emission suggests the occurrence of an one-way street energy transfer mechanism from the phthalocyanine to graphene oxide but not the other way around. We model this phenomenon through FRET where Förster radii between dye molecules and from dye to *nGO* are essential parameters. Be that as it may, there is a computational limitation on performing any electronic structure calculations regarding the photothermal agent, due to it being an extended system. Thus, absorption and emission spectra cannot be simulated, making it impossible to calculate the latterly mentioned radius. Bearing that in mind, we make it a parameter in our simulations. Results are shown in the following sections.

ρ_{dye} (g/L)	ρ_{nGO} (g/L)	Emission quenching (%)	
		Separate cuvette	Same cuvette
0.31	2.96	15.3	58.7
	6.30	31.4	70.5
	12.65	46.3	73.1
ρ_{dye} (g/L)	ρ_{nGO} (g/L)	Fluorescence (%)	
		Separate cuvette	Same cuvette
0.31	2.96	84.7	41.3
	6.30	68.6	29.5
	12.65	53.7	26.9

Table 4.1: Experimentally observed emission quenching and fluorescence intensity in separate and same cuvettes. Data provided by Professor Paterno.

4.2 Electronic structure

As mentioned in previous chapters, we obtained optimized geometries and normal mode frequencies for *AlClPc* ground and first excited states, which allowed for the simulation of absorption and emission spectra. Initially, we got these spectra using B3LYP functional in gas phase, due to it being an industrial standard. It does not have, however, any long range corrections, which might be relevant depending on the studied compound. Hence the use of ωB97XD functional to investigate the relevance of long range interactions for such molecules. For both functionals in any condition were used with 6-31G(d,p) basis.

Figure 4.3a shows the absorption spectra (S_0) for each functional displaying energy (in eV) vs its absorption cross section (in $Å^2$). Figure 4.3b shows the emission spectra (S_1) in an energy (in eV) vs differential emission rate (dimensionless) plot. Notably, for both electronic states, the shape of the spectrum is very well conserved. We can observe the intensities are slightly diminished when ωB97XD is used, as well as a small, yet visible, red shift. Table 4.2 displays all the numerical data obtained from the spectra shown in this section. Both absorption and emission spectra using B3LYP and ωB97XD in gas phase are in good agreement with experimentally obtained spectrum (shown in figure 4.1a).

In order to provide better similarities with the performed experiment, which had all compounds in ethanol solution, we accounted for the presence of ethanol using Polarization Continuum Model (PCM). Its effect can be more or less expressive depending on the employed functional. We performed PCM calculations for both B3LYP and ωB97XD and the same behavior was observed when compared to their gas phase counterparts. In figures 4.3c and 4.3d

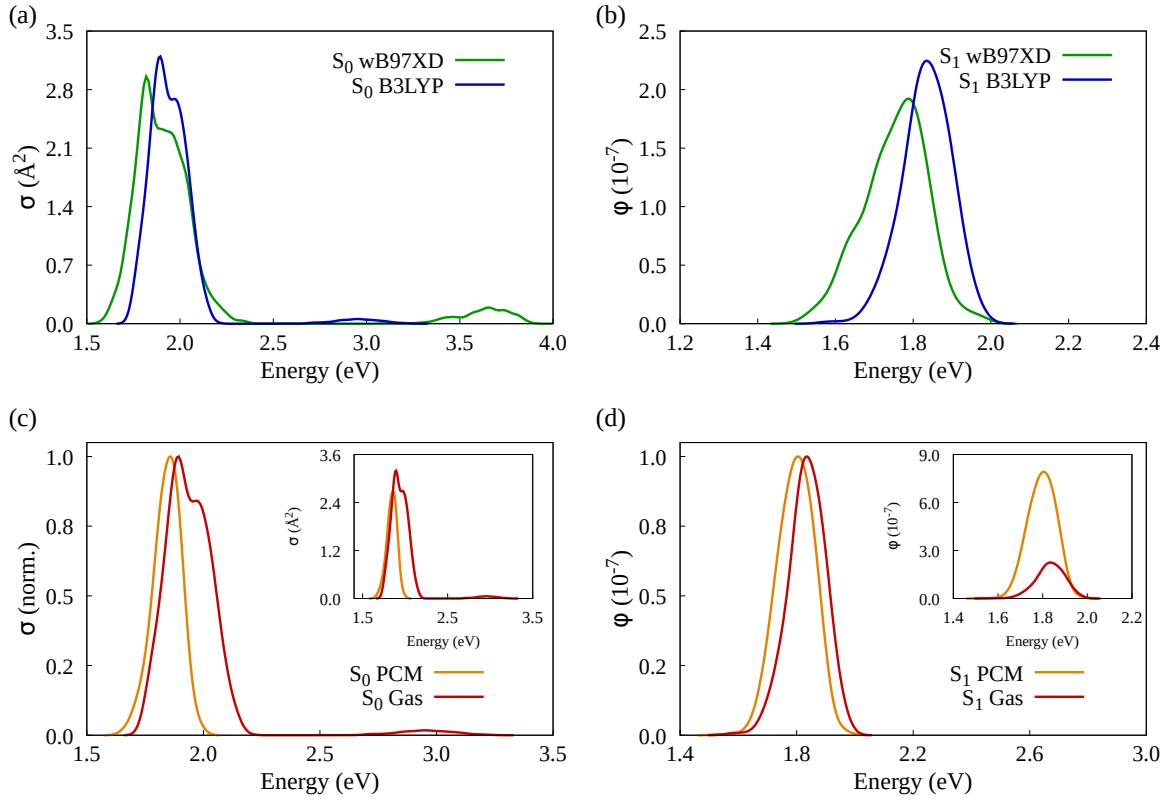

Figure 4.3: Absorption (a) and emission (b) spectra for AlClPc with B3LYP (blue) and ωB97XD (green) functionals. Normalized absorption (c) and emission (d) spectra for AlClPc using PCM method (orange) and in gas phase (red) with B3LYP functional. The insets in figures (4c) and (4d) represent the non-normalized spectra, displaying the difference of intensity seen with each electronic structure method

we make comparisons between gas phase and PCM related spectra when employing B3LYP functional. Drawing our attention to normalized absorption spectra (4.3c) we can see a smoother spectrum using PCM (orange), where the contribution seen around 2.0 eV in red is not visualized. Furthermore, a less expressive — when compared to the one resulting from different employed functionals — red shift is also observed. The inset presents the same spectra, but without any normalization, where we can observe PCM results in a diminished intensity of about 10% from peak to peak. Lastly, looking at the respective fluorescence spectra, the only expressive variation from PCM usage is a threefold increase in the differential emission rate (ϕ) compared to gas phase, as seen in the inset plot in figure 4.3d. The difference of intensities in both cases is

Method	S_0		S_1		
	$E_{S_0 \to S_1}$	E_{peak}	$E_{S_1 \to S_0}$	μ (a.u.)	E_{peak}
B3LYP (gas)		1.89	1.94	2.9	1.83
ωB97XD (gas)		1.81	1.82	3.2	1.78
B3LYP (PCM)		1.85	1.69	4.2	1.80
ωB97XD (PCM)		1.78	1.70	4.5	1.71
Experimental	-	1.88	-	-	1.92

Table 4.2: Vertical transition energies for *AlClPc* ($E_{S_0 \to S_1}$ in eV and spectral energies respective to maximum intensity (E_{peak}) in eV, as well as electric transition dipole moments from S_1 data in atomic units.

due to PCM model considering the molecule's refractive index (n). In the emission spectrum the dependence is with n^2, while absorption is with n^{-1}. The theoretical value for n can be determined as the square root of the dynamic dielectric constant, which is calculated by default with PCM. In gas phase spectra, we take $n = 1$.

Although the difference in calculation level (functional choice) does not seem to cause significant changes in spectral data, the resulting overlap might present changes, therefore altering the Förster radius. As mentioned in the previous section, a high R_F was expected. The panel displayed in figure 4.4 shows spectral overlaps for each calculation level: B3LYP in gas phase (a); ωB97XD in gas phase (b); B3LYP in ethanol solution (c); ωB97XD in ethanol solution (d).

We have pointed out a few changes in the spectra depending on the employed calculation method, but such changes occur hand-in-hand for S_0 and S_1. This translates into all methodologies yielding a large spectral overlap, translating into high Förster radii. Calculated exciton diffusion parameters obtained from the presented in this section are shown in table 4.3.

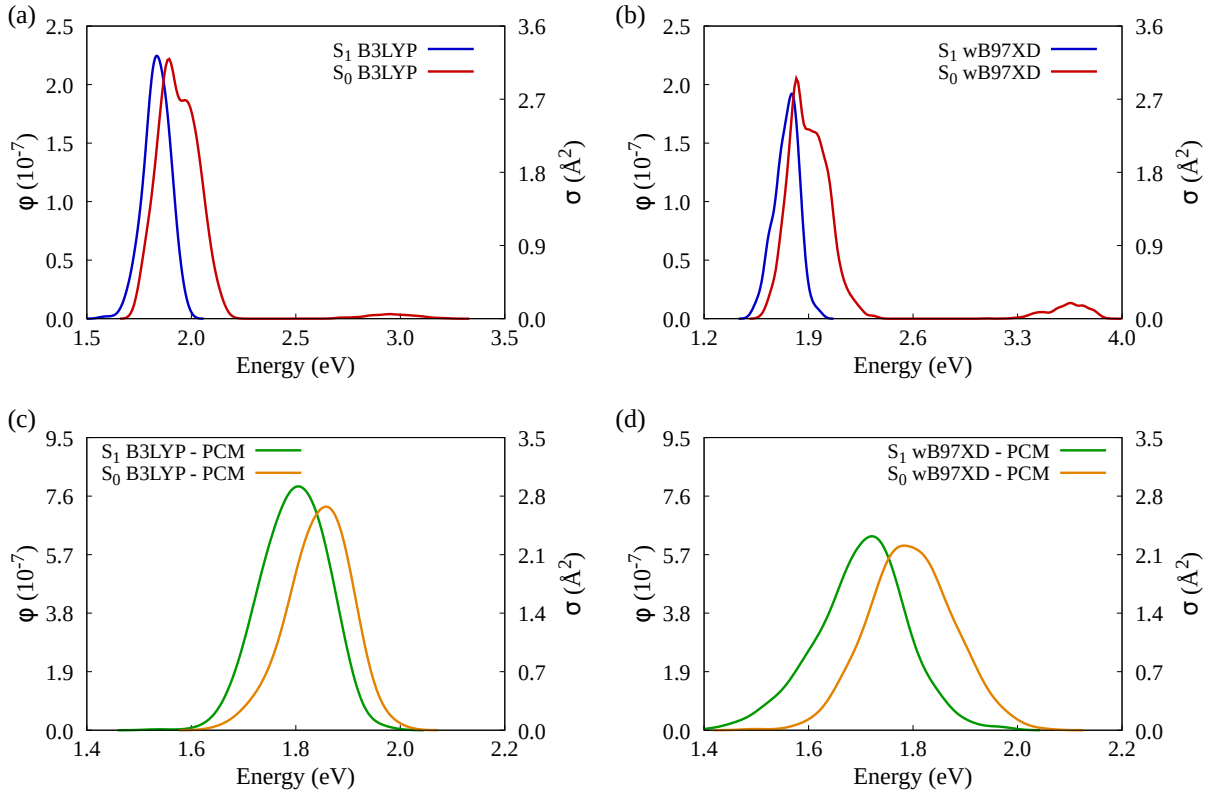

Figure 4.4: Absorption (red) and emission (blue) spectra for AlClPc with B3LYP (a) and ωB97XD (b) functionals in gas phase calculations. Absorption (orange) and emission (green) spectra for AlClPc using PCM method with B3LYP (c) and ωB97XD functionals.

Method	τ_{emi} (ns)	R_F (Å)	Estimated L_D (nm)			
			1D	2D	3D	Amorphous
B3LYP (gas)	17.9	91.7	449.5	292.2	209.4	180.6
ωB97XD (gas)	16.8	91.8	428.9	278.6	199.2	173.2
B3LYP (PCM)	4.9	89.7	343.6	222.7	158.4	140.8
ωB97XD (PCM)	5.1	87.8	309.5	200.4	142.3	127.3

Table 4.3: Exciton radiative lifetime (τ_{emi}) in nanoseconds. Förster radius R_F expressed in Å. Diffusion lengths (L_D) in nanometers for 1D, 2D, 3D crystal and amorphous structures.

4.3 Energy transfer dynamics — KMC

Kinetic Monte Carlo simulations were performed under several morphological conditions in order to obtain satisfactory results using experimental data as validation.

4.3.1 Filter effect

The first experimental behavior (shown in figure 4.2) we investigated was quenching due to *nGO* acting as a light filter to *AlClPc* when the compounds are in different cuvettes. We imitate such effect by reducing the amount of excitons in each simulation, which were calculated from the spectral area for different *nGO* concentrations. This data is shown in table 4.1. To exemplify, for $\rho_{nGO} = 2.96$ g/L, the simulation was performed with 8.47×10^5 excitons, while when $\rho_{nGO} = 6.30$ g/L we had around 6.86×10^5 excitons. Fluorescence spectra respective to the dye for each *nGO* concentration are shown in figure 4.5.

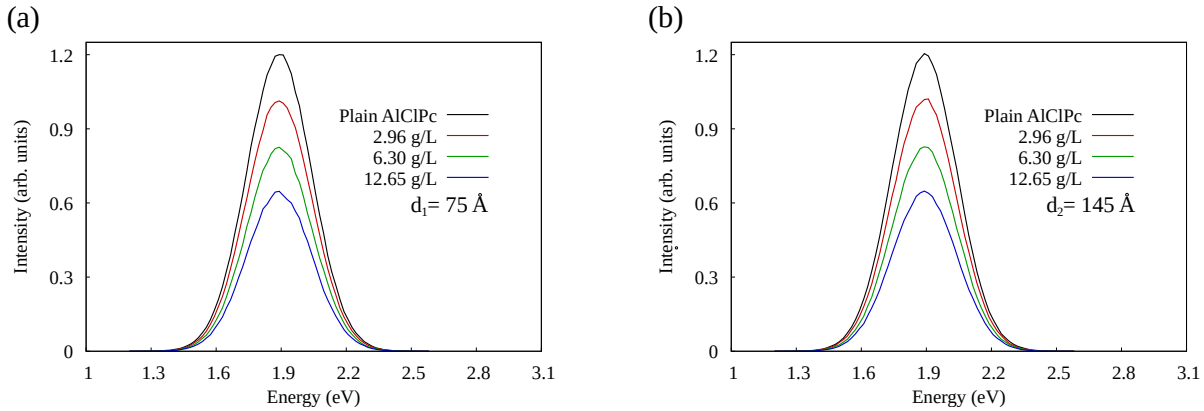

Figure 4.5: Plain *AlClPc* fluorescence spectra is shown black. *AlClPc* fluorescence spectra in the presence of *nGO* in separate cuvette is displayed in red (2.96 g/L), green (6.30 g/L) and blue (12.65 g/L). In (a) we presented the data for the case of $\rho_{dye} = 2.26$ g/L and in (b) for $\rho_{dye} = 0.31$ g/L. Spectra in (b) represent a simulated counterpart to figure4.2a (performed in separate cuvettes).

The fluorescence spectra shown above carry a remarkable resemblance to the ones

obtained experimentally. A noteworthy observation is how the filter effect does not depend on the existing morphology in the dye sample, addressing the similarity between 4.5(a) and 4.5(b).

Furthermore, in chapter 3 we discussed how system morphology was built as well as what necessary corrections were implemented in the simulation's time step. Using $\alpha = 10^{-3}$ we were able to produce satisfactory TRPL spectra for all concentrations of dye and *nGO*. In figure 4.6 we show TRPL spectra for $\rho_{dye} = 2.26$ g/L (intermolecular distance of 75 Å and all three *nGO* concentrations, making note of the corresponding cubic lattice's side length (L_{box}). The intensity of emission is represented in the percentage of excitons inserted in the simulation that fluoresced. The calculated diffusion lengths in 4.6 were of 1535 Å (a), 1185 Å (b) and 932 Å (c) and as expected, they were invariant with the change in the α.

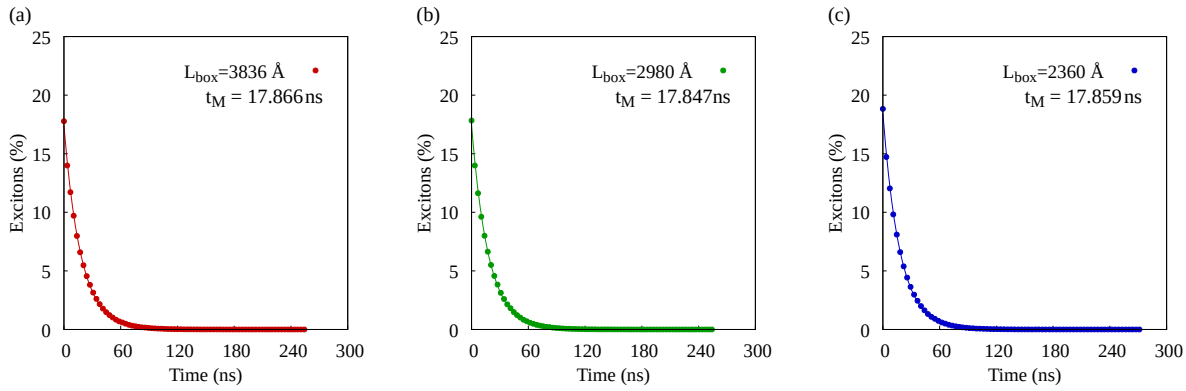

Figure 4.6: Chloroaluminum phthalocyanine TRPL spectra with $\rho_{dye} = 2.26$ g/L. In red (a) we show TRPL when $\rho_{nGO} = 2.96$ g/L, with corresponding $L_{box} = 3836$ Å. In green (b) we show TRPL when $\rho_{nGO} = 6.30$ g/L, with corresponding $L_{box} = 2980$ Å. In blue (c) we show TRPL when $\rho_{nGO} = 12.65$ g/L, with corresponding $L_{box} = 2360$ Å.

Concurrently, we performed the same calculations for the case of $\rho_{dye} = 0.31$ g/L (intermolecular distance of 145 Å). Results are shown in figure 4.7. Satisfactory monoexponential fits yielded exciton radiative lifetimes higher than what was calculated from the emission spectrum, but in an maximum error range of 2.2%, which is still in very good agreement. The use of a

smaller α could have led to slightly more accurate fitting parameters, however, the increase in computational time to run corresponding KMC simulations makes it unadvantageous. Diffusion lengths were also calculated: 1885 Å (a), 1452 Å (b) and 1134 Å (c).

It is worth recalling that none of the results in this section had aggregation effects implemented in the system's morphology, nor was the possibility of exciton transfer from *AlClPc* considered due to us being in a separate cuvette scenario.

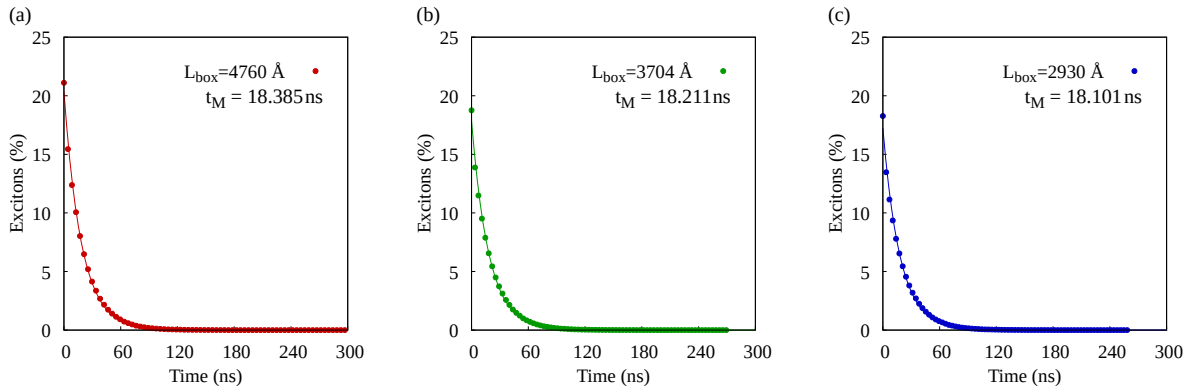

Figure 4.7: Chloroaluminum phthalocyanine TRPL spectra with $\rho_{dye} = 0.31$ g/L. In red (a) we show TRPL when $\rho_{nGO} = 2.96$ g/L, with corresponding $L_{box} = 4760$ Å. In green (b) we show TRPL when $\rho_{nGO} = 6.30$ g/L, with corresponding $L_{box} = 3704$ Å. In blue (c) we show TRPL when $\rho_{nGO} = 12.65$ g/L, with corresponding $L_{box} = 2930$ Å.

4.3.2 NGO exciton collection

From this moment forth all following results were obtained taking exciton transfer between *AlClPc* and *nGO* into consideration. Filter effect results were also taken into account determining the number of excitons in each simulation. The initial quenching observed in separate cuvette is included in the amount of quantified quenching when excitons can reach the photothermal agent. Owing to the fact the such excitons cannot return to *AlClPc* molecules to be recombined — one-way street in FRET —, we shall label them as *collected*. Once an

exciton is collected, the simulation is over and the next round begins.

Using the average intermolecular distances between dyes of 75 Å ($\rho_{dye} = 2.26$ g/L) and 145 Å ($\rho_{dye} = 0.31$ g/L) we increased the Förster radius relative to the excitons being transferred from dye to *nGO* in order to quantify corresponding quenching. In figure 4.8 we show quenching progression as R_F increases (a) as well as the corresponding fluorescence (b) for each *nGO* concentration with $\rho_{dye} = 2.26$ g/L (intermolecular distance 75 Å). Notably, as the Förster radius increases, the behavior differs per graphene oxide concentration. For the lowest concentration, an increase in R_F from 90 Å to 200 Å leads to increased quenching, however plateauing at approximately 30%. At the same time, for the other two *nGO* concentrations, the percentage of collected excitons remains the same regardless of the Förster radius. Such behavior implies that every exciton that could reach the *AlClPc-nGO* interface was already doing so and being collected for a radius of 90 Å. Analysis over the corresponding fluorescence shows that excitons are not being collected nearly as much. The dashed lines in figure 4.8b represent where experimental fluorescence is.

Following the same procedure for the case of $\rho_{dye} = 0.31$ g/L (intermolecular distance of 145 Å), we can see a different behavior in exciton collection, as shown in figure 4.9a. The collection increases with the Förster radius in every *nGO* concentration, reaching their respective plateau at approximately $R_F = 200$ Å. Corresponding fluorescence is shown in figure 4.9b. Comparatively to the previous dye concentration, fluorescence decreases more as R_F increases, although still not reaching experimental levels.

As previously stated, all experimental measurements were performed in a dye concentration of 0.31 g/L. In addition, the simulated counterparts without any molecular aggregation for

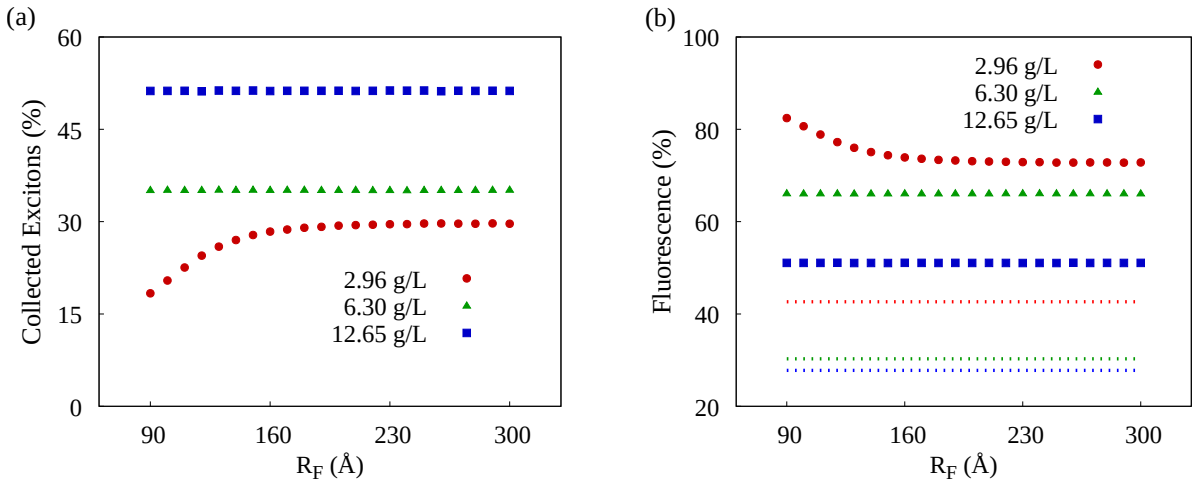

Figure 4.8: Collected excitons (a) and dye fluorescence (b) per *nGO* concentration when $\rho_{dye} = 2.26$ g/L. Dashed lines represent corresponding experimental reference.

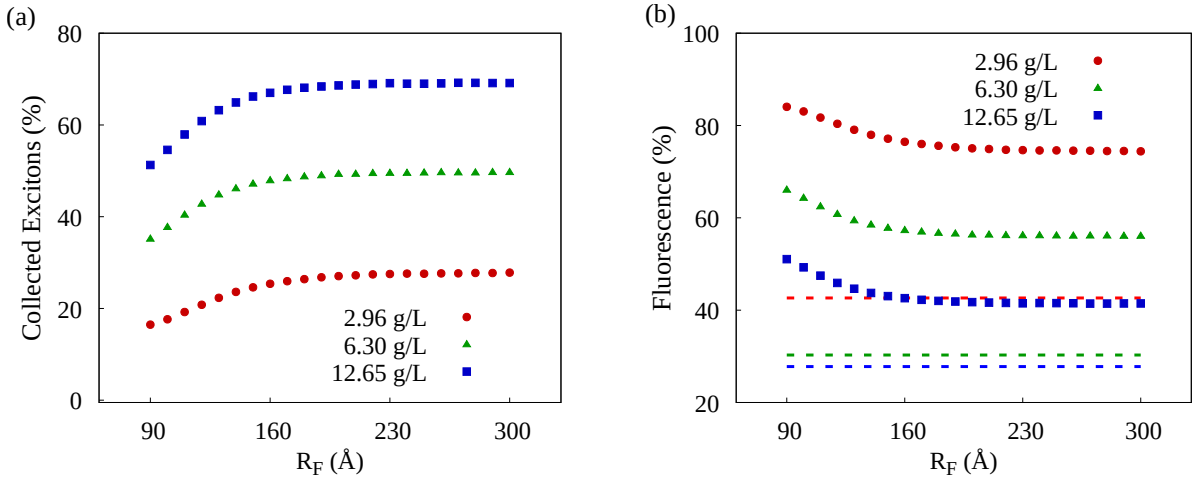

Figure 4.9: Collected excitons (a) and dye fluorescence (b) per *nGO* concentration when $\rho_{dye} = 0.31$ g/L. Dashed lines represent corresponding experimental reference.

this concentration provided results that do not get closer to experimental ones. Hence, we implemented molecular aggregation based on a geometric progression described in chapter 3 for this particular dye concentration. Simulated results are described below.

Molecular aggregation

In this section we considered molecular aggregation reaching from 2% ($q = 0.98$) to 20% ($q = 0.80$). The Förster radius parameter varied from 80 Å to 100 Å. Figure 4.10 displays the fluorescence percentage according to aggregation decrease for each *nGO* concentration.

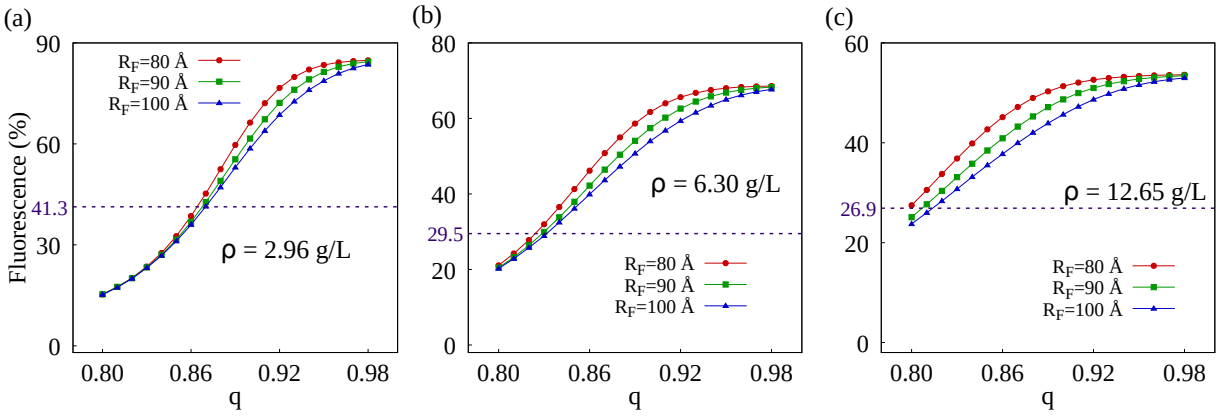

Figure 4.10: Fluorescence in exciton percentage per degree of aggregation. Förster radius between dye and *nGO* varies from 80 Å to 100 Å. Average intermolecular distance of 145 Å($\rho_{dye} = 0.31$ g/L).

In the horizontal axis we have q, which is the ratio of the aggregation geometric progression. The vertical axis accounts for the percentage of excitons that fluoresced in the simulation. From (a) through (c) we have *nGO* concentrations $\rho_{nGO} = 2.96$ g/L, $\rho_{nGO} = 6.30$ g/L and $\rho_{nGO} = 12.65$ g/L, respectively. The lines in red represent the data for when $R_F = 80$ Å, while the ones in green and blue display the data for $R_F = 90$ Å and $R_F = 100$ Å, respectively. The dashed lines in each plot represents the experimentally obtained fluorescence in that concentration, according to the surface area under the spectra.

In figure 4.10a we can observe that the Förster radius makes no significant difference in the degree of aggregation that matches experimental fluorescence, placing $q \approx 0.93$ for R_F of 90 Å. While in figure 4.10b even if all three values for R_F can reproduce experimental

fluorescence, a larger gap between the corresponding curves is observed, yielding a range of possible molecular aggregation. In this case, for $R_F = 90$ Å, corresponding aggregation is identified in $q \approx 0.84$. Nonetheless, in figure 4.10c, one can notice that no fluorescence produced with a dye-*nGO* radius of 80 Å matches experimental data. Furthermore, we can see a corresponding molecular aggregation range with $q \approx 0.81$ for $\rho_{nGO} = 12.65$ g/L. Provided that the size of the cubic lattice changes considerably with *nGO* presence, it is reasonable to expect different degrees of aggregation. The number of molecules should alter how many of which suffer aggregation, which explains different values of q.

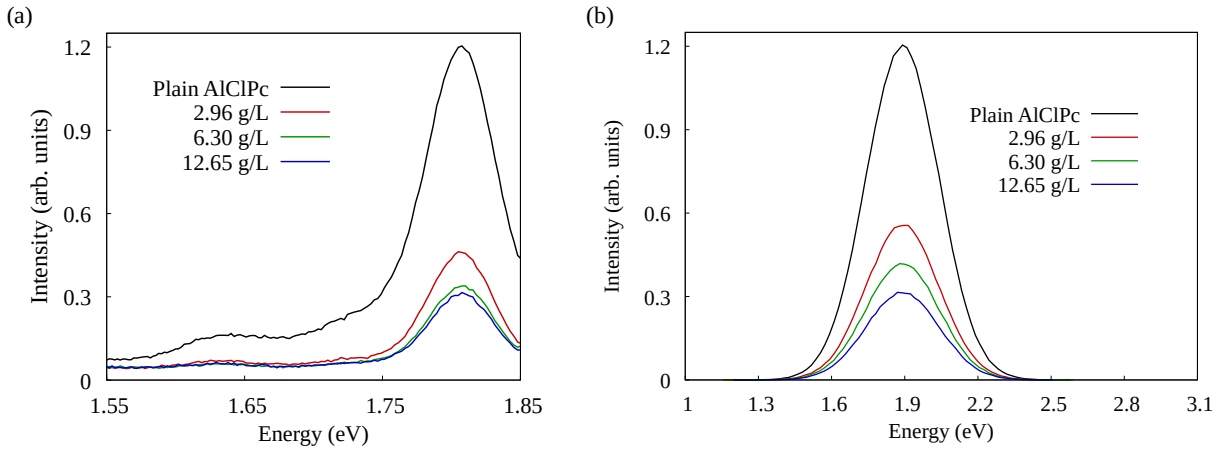

Figure 4.11: Experimentally obtained *AlClPc* fluorescence spectra in the same cuvette for different *nGO* concentrations and $\rho_{dye} = 0.31$ g/L (a). Simulated *AlClPc* fluorescence spectra taking molecular aggregation and exciton transfer between the dye and *nGO* into consideration for the same concentrations (b).

Now that we have identified the level of aggregation in each concentration, we obtained the corresponding emission spectra for $R_F = 90$ Å, which is shown in figure 4.11b, while 4.11a shows the corresponding experimental spectra. The simulated intensity was put in the same scale as the experimental spectra for comparison. One can observe the quenching behavior in very good agreement with what was obtained experimentally. The lowest *nGO* concentration

($\rho_{nGO} = 2.96$ g/L), displayed in red, is enough to cause intense molecular aggregation. Such aggregation reduces dye's fluorescence by over 50% in combination with the filter effect. By comparing the observed quenching between the lowest and highest *nGO* concentrations we see a difference of less than 15% in fluorescence for a six-fold increase in *nGO* concentration.

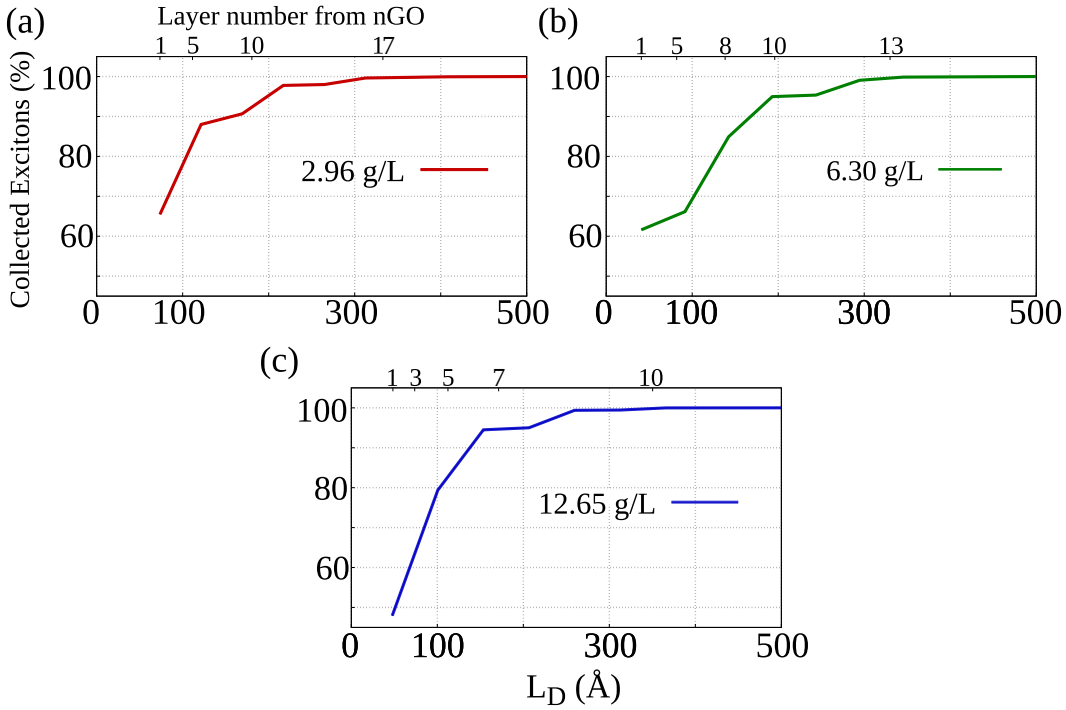

Figure 4.12: Diffusion length of collected excitons for the simulated cases that matched experimental data. In (a) we have $\rho_{nGO} = 2.96$ g/L, $q = 0.93$ and $\rho_{dye} = 0.31$ g/L. In (b) we have $\rho_{nGO} = 6.30$ g/L, $q = 0.84$ and $\rho_{dye} = 0.31$ g/L and in (c) $\rho_{nGO} = 12.65$ g/L, $q = 0.81$ and $\rho_{dye} = 0.31$ g/L.

Given that molecular aggregation was paramount to excitons being transferred from the dye to *nGO*, we investigated the diffusion length of collected excitons. Figure 4.12 shows the distribution of diffusion length in the inferior horizontal axis, while in the vertical axis we see the cumulative percentage of collected excitons. In the superior horizontal axis we label the distance of some of the layers starting from the *nGO*, i.e, the fifth layer of dye from *nGO* in (a) is at almost 100 Å from the *nGO*. In figure 4.12a the data corresponds to the case of $\rho_{nGO} =$

2.96 g/L, $q = 0.93$ and $\rho_{dye} = 0.31$ g/L, while in 4.12b we have $\rho_{nGO} = 6.30$ g/L, $q = 0.84$ and $\rho_{dye} = 0.31$ g/L and in 4.12c we have $\rho_{nGO} = 12.65$ g/L, $q = 0.81$ and $\rho_{dye} = 0.31$ g/L. We can observe that in all cases, over 80% of collected excitons are generated, in average, in the first half of dye layers. From the morphologies presented in chapter 3, for the lowest *nGO* concentration, we have 17 layers of dye between the central molecule and the *nGO* face. Notably, around 90% of all excitons were generated no farther than the 10th layer starting from *nGO*. This goes to show that quenching at this intensity can only be seen due to molecular aggregation and that dye molecules that end up being separated by larger distances do not significantly contribute to fluorescence reduction.

CHAPTER 5

CONCLUSION

In this work, we studied exciton dynamics in chloroaluminum phthalocyanine molecules and graphene oxide sheets. Based on external experimental results, we developed a model for energy transfers between the two compounds. In order to do that, we investigated the photodynamic agent's electronic structure as the solution to the electronic problem obtained from using the Born-Oppenheimer approximation within the many body problem. Utilizing DFT, we were able to obtain optimized geometries and normal mode frequencies for the ground and first excited states in different calculation levels, as well as possible transitions. Performing the same electronic structure calculations to graphene oxide was not possible due to computational limitations surrounding the simulation of extended systems. In regards to morphology, the difference in size between the dye and *nGO* indicates an elevated number of atoms in the latter, which prevents *ab-initio* calculations from being performed. Relating to the photodynamic agent, from S_0 and S_1 calculations, we simulated corresponding absorption and emission spectra

via the nuclear ensemble method. Such method takes a semi-classical approximation into account, in which the nuclei in the many body problem are treated classically while the electrons are governed by Schrödinger's time-dependent equation. Comparison between experimental and simulated spectra points to a good agreement regarding their general shape and energy range, as well as their Stokes shift. We employ the Förster formalism to describe the dynamics involving energy transfer processes in the aforementioned agents. As a direct result from the dye's simulated spectra, we calculated its Förster radius knowing the overlap. Furthermore, exciton radiative lifetime was obtained through integrating the fluorescence spectra. Although the numerical difference between experimental and simulated lifetime is considerable, both are in the same order of magnitude, which presents it as a satisfactory result. Said agreement suggests that *AlClPc* is not affected by non-radiative phenomena.

The experimental work was performed using ethanol diluted solutions of phthalocyanine and graphene oxide in different concentrations. Using stoichiometry, typical intermolecular distances were ascertained. Average intermolecular distances between dyes were estimated to be 75 Å and 145 Å for $\rho_{dye} = 2.26$ g/L and $\rho_{dye} = 0.31$ g/L, respectively. The latter distance is superior to the molecule's Förster radius — which suggests reduced exciton transfer and elevated recombination — and it is considered to be unusually elevated for organic molecules. However, experimental results were not reproduced under these conditions. Due to typical electronic structure of aromatic compounds, molecular aggregation is expected to occur, mostly through π-staking. That said, an aggregation model where dye molecules closer to *nGO* are brought together was proposed. Different *nGO* concentrations were recreated by changing the size of the simulated lattices. Higher *nGO* concentrations translated into smaller lattices because

it meant less dye molecules proportional to the amount of graphene oxide.

Applying the described morphological model, exciton dynamics was investigated using a Kinetic Monte Carlo algorithm. Provided that we cannot simulate graphene oxide's absorption spectrum, Förster radius from *AlClPc* to *nGO* was used as a parameter, which ranged from 80 Å to 100 Å. In addition, the calculated amount of molecules in the morphological model led to different sized lattices for each *nGO* concentration. In respect to the two interactions between photosensitizing agents identified in the experimental setup: the first was obtained with the solutions in different cuvettes. Such physical barrier led to the *nGO* solution acting as a light filter, reducing the dye's light absorption and consequent fluorescence; reduction which was observed as a small quenching in the fluorescence spectrum. The other effect was noticed when measurements were performed with both solutions in the same cuvette, allowing for them to interact with each other. In this case, spectral quenching is intensified with the increased presence of *nGO*. In order to simulate the first effect, we considered a null Förster radius between *AlClPc* and *nGO*. As for the second one, the simulation was performed for different values of said Förster radius and different degrees of molecular aggregation. Using experimental results as validation we were able to estimate the parametric Förster radius and different degrees of aggregation observed in each *nGO* concentration.

Finally, we were able to suggest that molecular aggregation between dye molecules due to the presence of graphene oxide caused enhanced exciton absorption by *nGO* as a competing mechanism to singlet exciton transfer within *AlClPc* sites. Furthermore, we showed that whatever transfer occurs between non-aggregated molecules hardly affects the observed quenching. With that in mind, one could infer that such quenching may be avoidable if the agents are biocompatible.

However, experimental works were performed with and without the use of Pluronic-127 polymer and it made no difference in the aforementioned attenuating effects. Thus, other compatibility methods would need to be investigated while trying to prevent the escape of excitons from dye to graphene oxide.

The study here described can be further improved by employing a less artificial aggregation model as well as a genetic algorithm to ascertain the precise level aggregation in different models and their corresponding Förster radius. The protocol used in electronic structure calculations can easily be extended to other photosensitizing agents.

CHAPTER 6

APPENDIX A

Many-body problem

In the context of a molecular compound, the many-body problem is often identified. Let us consider a molecular system with N electrons and M nuclei, indexed by $\{i, j, ...\}$ and $\{A, B, ...\}$, respectively. Our system is shown in figure 6.1, in which $\vec{r}_i$ is the position vector for the ith electron, $\vec{r}_{ij}$ is the distance between the ith and the jth electron, $\vec{R}_A$ is the position vector for the Ath nucleus, $\vec{R}_{AB}$ is the distance between the Ath and Bth nuclei and $\vec{R}_{Ai}$ is the distance between the Ath nucleus and the ith electron. Schrödinger's non-relativistic time-independent equation is

$$\hat{H}\Psi = E^T\Psi \tag{6.1}$$

where $\hat{H}$ is the Hamiltonian operator and E^T is the eigenvalue for the system's total energy. Taking into account that the nuclei are positively charged, we can express the Hamiltonian as

$$\hat{H} = \hat{T}_n + \hat{T}_e + \hat{V}_{ee} + \hat{V}_{nn} + \hat{V}_{en} \tag{6.2}$$

with $\hat{T}_n$ and $\hat{T}_e$ being the kinetic energy operators for the nuclei and for the electrons, respectively. In addition, $\hat{V}_{nn}$ is the operator for the interaction between nuclei, $\hat{V}_{ee}$ accounts for the interaction between electrons and $\hat{V}_{en}$ considers the interaction energy between electrons and nuclei.

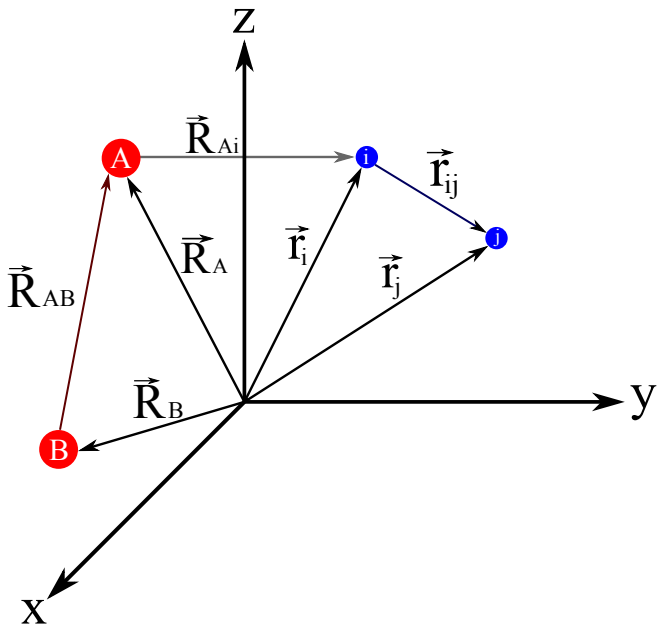

Figure 6.1: Schematic representation of the many-body problem for N electrons (i,j,...) and M nuclei (A,B,...).

We define the kinetic energy operator $\hat{T}$ in terms of the linear momentum operator $\hat{P}$,

$$\hat{T} = \frac{\hat{P}^2}{2m} \tag{6.3}$$

which is, in turn, defined by $\hat{P} = -i\hbar\vec{\nabla}$ when projected into the three dimensional position

space. Thus,

$$\hat{T} = \frac{(-i\hbar\vec{\nabla})\cdot(-i\hbar\vec{\nabla})}{2m} = -\frac{\hbar^2\nabla^2}{2m}. \tag{6.4}$$

Considering a purely Coulombic interaction between charges, the remaining operators are, in atomic units ($\hbar = m_e = e = k_e = 1$), expressed by

$$\hat{T}_n = -\frac{\hbar^2}{2}\sum_{A=1}^{M}\frac{\nabla_A^2}{m_A} = -\frac{1}{2}\sum_{A=1}^{M}\frac{\nabla_A^2}{m_A} \tag{6.5}$$

$$\hat{T}_e = -\frac{\hbar^2}{2m_e}\sum_{i=1}^{N}\nabla_e^2 = -\frac{1}{2}\sum_{i=1}^{N}\nabla_e^2 \tag{6.6}$$

$$\hat{V}_{ee} = \sum_{i=1}^{N}\sum_{j>i}^{N}k_e\frac{e^2}{r_{ij}} = \sum_{i=1}^{N}\sum_{j>i}^{N}\frac{1}{r_{ij}} \tag{6.7}$$

$$\hat{V}_{nn} = \sum_{A=1}^{M}\sum_{B>A}^{M}k_e\frac{(Z_Ae)(Z_Be)}{R_{AB}} = \sum_{A=1}^{M}\sum_{B>A}^{M}\frac{Z_AZ_B}{R_{AB}} \tag{6.8}$$

$$\hat{V}_{en} = -\sum_{A=1}^{M}\sum_{i=1}^{N}k_e\frac{Z_Ae^2}{R_{Ai}} = -\sum_{A=1}^{M}\sum_{i=1}^{N}\frac{Z_A}{R_{Ai}} \tag{6.9}$$

where we have already eliminated twice accounted interactions with the second sum in (6.7) and (6.8). The eigenfunction Ψ depends on the position sets for all electrons, $\{\vec{r}\}$, and nuclei $\{\vec{R}\}$,

$$\hat{H}\Psi(\{\vec{r}\};\{\vec{R}\}) = E^T\Psi(\{\vec{r}\};\{\vec{R}\}). \tag{6.10}$$

Hence, writing the Hamiltonian (6.1) becomes,

$$-\frac{1}{2}\sum_{A=1}^{M}\frac{\nabla_A^2}{m_A}\Psi + -\frac{1}{2}\sum_{i=1}^{N}\nabla_e^2\Psi + \sum_{i=1}^{N}\sum_{j>i}^{N}\frac{1}{r_{ij}}\Psi + \sum_{A=1}^{M}\sum_{B>A}^{M}\frac{Z_AZ_B}{R_{AB}}\Psi - \sum_{A=1}^{M}\sum_{i=1}^{N}\frac{Z_A}{R_{Ai}}\Psi = E^T\Psi. \tag{6.11}$$

Born-Oppenheimer approximation

Note that (6.11) is a differential equation that can only be solved using approximations. The first approximation to be done is to take advantage of separation of variables in Ψ, such as

$$\Psi(\{\vec{r}\};\{\vec{R}\}) = \psi_e(\{\vec{r}\};\{\vec{R}\})\chi_n(\{\vec{R}\}) \tag{6.12}$$

in which ψ_e is related to electron movement and χ_n accounts for nuclei movement. However, ψ_e is parametrically dependent on $\{\vec{R}\}$, that is, comparatively to $\{\vec{r}\}$, $\{\vec{R}\}$ is seen as a constant. This particular choice of variable separation reflects the *adiabatic approximation* for nuclei movement, where due to the considerable difference between electron masses and nuclei masses, one can assume that during the time it takes for an electron to move, the nucleus remains still. To summarize, this means that for obtaining the eigenfunction $\psi_e(\{\vec{r}\};\{\vec{R}\})$ we have to consider that there is no movement for the nuclei.

The Born-Oppenheimer approximation is based on employing the *adiabatic approximation* in $\hat{T}_n$ applied to Ψ, like so,

$$\hat{T}_n\Psi = -\frac{1}{2}\sum_{A=1}^{M}\frac{\nabla_A^2}{m_A}[\psi_e(\{\vec{r}\};\{\vec{R}\})\chi_n(\{\vec{R}\})] \tag{6.13}$$

where the Laplace operator application stays as

$$\begin{aligned}\nabla_A^2[\psi_e(\{\vec{r}\};\{\vec{R}\})\chi_n(\{\vec{R}\})] &= \vec{\nabla}_A \cdot [\vec{\nabla}(\psi_e\chi_n)] \\ &= \vec{\nabla}_A \cdot (\chi_n\vec{\nabla}_A\psi_e + \psi_e\vec{\nabla}_A\chi_n) \\ &= \chi_n\nabla_A^2\psi_e + \psi_e\nabla_A^2\chi_n + 2\vec{\nabla}_A\chi_n\vec{\nabla}_A\psi_e\end{aligned} \tag{6.14}$$

in which, following the aforementioned parametric dependence of ψ_e with $\{\vec{R}\}$, the terms $\vec{\nabla}_A\psi_e$ and $\nabla_A^2\psi_e$ are null. Hence,

$$\hat{T}_n\Psi = -\frac{\psi_e}{2}\sum_{A=1}^{M}\frac{\nabla_A^2\chi_n}{m_A} \tag{6.15}$$

such that, using that in (6.11) and dividing the equation for $\psi_e\chi_n$, we conclude

$$-\frac{1}{2}\sum_{A=1}^{M}\frac{1}{\chi_n}\frac{\nabla_A^2\chi_n}{m_A} - \frac{1}{2}\sum_{i=1}^{N}\frac{\nabla_e^2\psi_e}{\psi_e} + \sum_{i=1}^{N}\sum_{j>i}^{N}\frac{1}{r_{ij}} + \sum_{A=1}^{M}\sum_{B>A}^{M}\frac{Z_AZ_B}{R_{AB}} - \sum_{A=1}^{M}\sum_{i=1}^{N}\frac{Z_A}{R_{Ai}} = E^T. \tag{6.16}$$

Choosing $-\varepsilon$ as our separation constant, we can obtain the Electronic Schrödinger equation,

$$\boxed{-\frac{1}{2}\sum_{i=1}^{N}\nabla_e^2\psi_e + \sum_{i=1}^{N}\sum_{j>i}^{N}\frac{\psi_e}{r_{ij}} - \sum_{A=1}^{M}\sum_{i=1}^{N}\frac{Z_A}{R_{Ai}}\psi_e + \sum_{A=1}^{M}\sum_{B>A}^{M}\frac{Z_AZ_B}{R_{AB}}\psi_e = \varepsilon\psi_e} \tag{6.17}$$

where $\varepsilon = \varepsilon(\{\vec{R}\})$, and the Nuclear Schödinger equation,

$$\boxed{-\frac{1}{2}\sum_{A=1}^{M}\frac{\nabla_A^2\chi_n}{m_A} + \varepsilon(\{\vec{R}\})\chi_n = E^T\chi_n}. \tag{6.18}$$

Through the adiabatic approximation, we can understand that for each specific nuclear

geometric configuration (or that for each parametric $\{\vec{R}\}$ in (6.17)), we obtain a particular solution for (6.17). Multiple solutions form the potential energy surface for different inter nuclear distances, or simply put, to different molecular geometric conformations.

CHAPTER 7

APPENDIX B

Density Functional Theory

As our starting point, let's take the electronic Hamiltonian operator obtained from the Born-Oppenheimer approximation,

$$\hat{H}_{ele} = \hat{T}_e + \hat{V}_{en} + \hat{V}_{ee} \tag{7.1}$$

$$\hat{H}_{ele} = -\sum_{i=1}^{N} \nabla_i^2 - \sum_{i=1}^{N}\sum_{A=1}^{M} \frac{Z_A}{r_{iA}} + \sum_{i=1}^{N}\sum_{j\neq i}^{N} \frac{1}{r_{ij}} \tag{7.2}$$

where $\hat{T}_e$ is the kinetic energy operator for electrons, $\hat{V}_{en}$ is the potential interaction between the i-th electron and the A-th nucleus and $\hat{V}_{ee}$ is the attraction potential due to the interaction between two electrons. We can rewrite the Hamiltonian in terms of the sum of one-electron and

two-electron operators, such as,

$$\hat{H}_{ele} = \hat{O}_1 + \hat{O}_2 = \sum_{i=1}^{N} (T(i) + \vartheta(i)) + \sum_{i=1}^{N} \sum_{j \neq i}^{N} \frac{1}{r_{ij}} \tag{7.3}$$

in which,

$$\vartheta(i) = -\sum_{A=1}^{M} \frac{Z_A}{r_{iA}} \tag{7.4}$$

Notice that such Hamiltonian depends only on the positions and atomic numbers of the nuclei and the total number of electrons. Such dependence suggests the electron density ρ as an observable we can investigate in practical terms without necessarily having to learn the form of the wave function. When integrated over all space, the electron density gives the total number of electrons,

$$N = \int \rho(\vec{r}) d\vec{r}. \tag{7.5}$$

For a known wave function ψ, that is, a solution to $\hat{H}_{ele}$, the energy can be expressed as a functional of ψ, such as

$$E[\psi] = \langle \psi | \hat{H}_{ele} | \psi \rangle = \langle \psi | \hat{O}_1 + \hat{O}_2 | \psi \rangle \tag{7.6}$$

In the following steps, we will detail the mathematical tools needed to prove the anchoring theorems of Density Functional Theory.

Mathematical formalism

From Mechanical Statistics, the density operator of a system is defined as,

$$\gamma = \sum_k |k\rangle \langle k| \tag{7.7}$$

where k indexes all the possible states in which the system can be found. In our case, if ψ is the complete solution for $\hat{H}_{ele}$, it is also the only possible state, which means the density operator can be written as

$$\gamma = |\psi\rangle \langle \psi| \tag{7.8}$$

Using that definition, one can build its matrix element,

$$\gamma(\vec{x}_1, \vec{x}'_1, \vec{x}_2, \vec{x}'_2, ..., \vec{x}_N, \vec{x}'_N) = \langle \vec{x}'_1, \vec{x}'_2, ..., \vec{x}'_N | \, |\psi\rangle \langle \psi| \, |\vec{x}_1, \vec{x}_2, ..., \vec{x}_N\rangle \tag{7.9}$$

$$= \psi(\vec{x}'_1, \vec{x}'_2, ..., \vec{x}'_N) \psi^*(\vec{x}_1, \vec{x}_2, ..., \vec{x}_N) \tag{7.10}$$

where if $\vec{x}_i = \vec{x}'_i$, then

$$\gamma = |\psi(\vec{x}_1, \vec{x}_2, ..., \vec{x}_N)|^2 \tag{7.11}$$

recovering the idea of the probability density.

Considering the intrinsic properties of a non-local operator, we can project γ into elements that are not from the same vector space ($\vec{x}_i \neq \vec{x}'_i$). Knowing that i indexes different particles, we can assume the first k particles are not in the density operator's space and integrate

over all particles in that space but the first k in γ's space, such as,

$$\gamma_k(\vec{x}'_1,\vec{x}'_2,..,\vec{x}'_k,\vec{x}_1,\vec{x}_2,...,\vec{x}_k) = \binom{N}{k}\int d\vec{x}_{k+1}d\vec{x}_{k+2}...d\vec{x}_N\,\psi(\vec{x}'_1,\vec{x}'_2,..,\vec{x}'_k,\vec{x}_{k+1},\vec{x}_{k+2},...,\vec{x}_N)\times$$
$$\psi^*(\vec{x}_1,\vec{x}_2,..,\vec{x}_k,\vec{x}_{k+1},\vec{x}_{k+2},...,\vec{x}_N) \quad (7.12)$$

This particular integration defines the reduced density operator's matrix element to k-th order. For our focus in Density Functional Theory, we are only interested in $k = 1$ and $k = 2$. Reducing it to the first order ($k = 1$) yields,

$$\gamma_1(\vec{x}'_1,\vec{x}_1) = \frac{N!}{1!(N-1)!}\int d\vec{x}_2 d\vec{x}_3...d\vec{x}_N\,\psi(\vec{x}'_1,\vec{x}_2,...,\vec{x}_N)\psi^*(\vec{x}_1,\vec{x}_2,...,\vec{x}_N) \quad (7.13)$$

which we can integrate over spin obtaining,

$$\int d\omega_1\gamma_1(\vec{x}'_1,\vec{x}_1) = \rho_1(\vec{r}'_1,\vec{r}_1) \quad (7.14)$$

that, in the case of $\vec{r}'_1 = \vec{r}_1$, turns into the known electron density,

$$\rho_1(\vec{r}_1) = \int d\omega_1\vec{x}_1,\vec{x}_2,...,\vec{x}_N)\psi^*(\vec{x}_1,\vec{x}_2,...,\vec{x}_N) \Longrightarrow N = \int d\vec{r}_1\rho_1(\vec{r}_1) \quad (7.15)$$

Now for $k = 2$,

$$\gamma_2(\vec{x}'_1,\vec{x}'_2,\vec{x}_1,\vec{x}_2) = \frac{N!}{2!(N-2)!}\int d\vec{x}_3...d\vec{x}_N\,\psi(\vec{x}'_1,\vec{x}'_2,\vec{x}_3...,\vec{x}_N)\psi^*(\vec{x}_1,\vec{x}_2,\vec{x}_3,...,\vec{x}_N) \quad (7.16)$$

and, integrating it over the spin coordinate,

$$\int d\omega_1 d\omega_2 \gamma_2(\vec{x}_1', \vec{x}_2', \vec{x}_1, \vec{x}_2) = \rho_2(\vec{r}_1', \vec{r}_2', \vec{r}_1, \vec{r}_2) \tag{7.17}$$

where for $\vec{r}_1' = \vec{r}_1$ and $\vec{r}_2' = \vec{r}_2$ we can obtain $\rho(\vec{r}_1, \vec{r}_2)$. Integrating it,

$$\int d\vec{r}_1 d\vec{r}_2 \rho_2(\vec{r}_1, \vec{r}_2) = \frac{N(N-1)}{2} \tag{7.18}$$

which corresponds exactly to the number of electron pairs. We can associate the one and two-electron operators to ρ_1 and ρ_2, respectively.

The one-electron operator contribution to the energy can be written as

$$\langle \psi | \hat{O}_1 | \psi \rangle = \int d\vec{x}_1 d\vec{x}_2 ... d\vec{x}_N \psi^*(\vec{x}_1, \vec{x}_2, \vec{x}_3, ..., \vec{x}_N) \left(\sum_{i=1}^{N} \hat{O}_1(\vec{x}_1) \right) \psi(\vec{x}_1, \vec{x}_2, \vec{x}_3, ..., \vec{x}_N) \tag{7.19}$$

$$= N \int d\vec{x}_1 d\vec{x}_2 ... d\vec{x}_N \psi^*(\vec{x}_1, \vec{x}_2, \vec{x}_3, ..., \vec{x}_N) \hat{O}_1(\vec{x}_1) \psi(\vec{x}_1, \vec{x}_2, \vec{x}_3, ..., \vec{x}_N) \tag{7.20}$$

$$= \int d\vec{x}_1 \hat{O}_1(\vec{x}_1) \gamma_1(\vec{x}_1', \vec{x}_1)|_{\vec{x}_1' = \vec{x}_1} \tag{7.21}$$

$$= \int d\vec{r}_1 \hat{O}_1(\vec{r}_1) \rho_1(\vec{x}_1) \tag{7.22}$$

$$= \int d\vec{r}_1 \left(-\frac{1}{2} \nabla_i^2 + \vartheta(i) \right) \rho_1(\vec{r}_1). \tag{7.23}$$

Doing a similar procedure on the two-electron operator contribution in the energy, we

have

$$\langle\psi|\,\hat{O}_2\,|\psi\rangle = \int d\vec{x}_1 d\vec{x}_2 ... d\vec{x}_N \psi^*(\vec{x}_1,\vec{x}_2,\vec{x}_3,...,\vec{x}_N)\left(\sum_{i=1}^{N}\sum_{j\neq i}\hat{O}_2(\vec{x}_1,\vec{x}_2)\right)\psi(\vec{x}_1,\vec{x}_2,\vec{x}_3,...,\vec{x}_N) \tag{7.24}$$

$$= \frac{N(N-1)}{2}\int d\vec{x}_1 d\vec{x}_2 ... d\vec{x}_N \psi^*(\vec{x}_1,\vec{x}_2,\vec{x}_3,...,\vec{x}_N)\hat{O}_2(\vec{x}_1,\vec{x}_2)\psi(\vec{x}_1,\vec{x}_2,\vec{x}_3,...,\vec{x}_N) \tag{7.25}$$

$$= \int d\vec{x}_1 d\vec{x}_2 \hat{O}_2(\vec{x}_1,\vec{x}_2)\gamma_2(\vec{x}_1',\vec{x}_1,\vec{x}_2',\vec{x}_2)|_{\vec{x}_1'=\vec{x}_1;\vec{x}_2'=\vec{x}_2} \tag{7.26}$$

$$= \int d\vec{r}_1 d\vec{r}_2 \hat{O}_2(\vec{x}_1,\vec{x}_2)\rho_2(\vec{r}_1,\vec{r}_2) \tag{7.27}$$

However, by doing this, the energy is not uniquely defined by the electron density. To obtain a more expressive result, we can arrange,

$$\langle\psi|\,\hat{O}_2\,|\psi\rangle = \frac{N(N-1)}{2}\int d\vec{x}_1\left(\int d\vec{x}_2\hat{O}_2(\vec{x}_1,\vec{x}_2)d\vec{x}_3 ... d\vec{x}_N \psi^*(\vec{x}_1,\vec{x}_2,\vec{x}_3,...,\vec{x}_N)\psi(\vec{x}_1,\vec{x}_2,\vec{x}_3,...,\vec{x}_N)\right) \tag{7.28}$$

$$= \int d\vec{r}_1 \Theta_2(\vec{r}_1)\rho_1(\vec{r}_1) \tag{7.29}$$

leading to,

$$E[\rho] = \int\left(-\frac{1}{2}\nabla_i^2 + \vartheta(\vec{r}) + \Theta_2(\vec{r})\right)\rho(\vec{r}) \tag{7.30}$$

where have defined,

$$\Theta_2(\vec{r}_1) = \frac{N(N-1)}{2} \int d\omega_1 \left(\int d\vec{x}_2 \hat{O}_2(\vec{x}_1,\vec{x}_2) d\vec{x}_3 ... d\vec{x}_N \psi^*(\vec{x}_1,\vec{x}_2,\vec{x}_3,...,\vec{x}_N) \psi(\vec{x}_1,\vec{x}_2,\vec{x}_3,...,\vec{x}_N) \right) \tag{7.31}$$

From equation (7.30), we can visualize that the energy can be written as a functional of the electron density.

Hartree-Fock with electron density

We can also write the Hartree-Fock wave function in terms of the density operators. In the Hartree-Fock approximation, the wave function for the eletronic Hamiltonian is given by a single Slater's determinant, like so,

$$|\psi_{ele}^{HF}\rangle = \frac{1}{\sqrt{N!}} \sum_i (-1)^{\mathscr{P}_i} \mathscr{P}_i (\chi_1(1)\chi_2(2)...\chi_N(N)) \tag{7.32}$$

$$= |\chi_1(1)\chi_2(2)...\chi_N(N)\rangle \,. \tag{7.33}$$

Using $|\psi_{ele}^{HF}\rangle$ to define γ_1 and γ_2 yields,

$$\gamma_1(\vec{x}_1,\vec{x}_1') = \sum_i^N \chi_i(\vec{x}_1') \chi_i^*(\vec{x}_1) \tag{7.34}$$

and

$$\gamma_2(\vec{x}_1,\vec{x}_2,\vec{x}_1',\vec{x}_2') = \frac{1}{2}\left(\gamma_1(\vec{x}_1,\vec{x}_1')\gamma_1(\vec{x}_2,\vec{x}_2') - \gamma_1(\vec{x}_2,\vec{x}_1')\gamma_1(\vec{x}_1,\vec{x}_2')\right) \tag{7.35}$$

$$= \frac{1}{2}\begin{vmatrix} \gamma_1(\vec{x}_1,\vec{x}_1') & \gamma_1(\vec{x}_1,\vec{x}_2') \\ \gamma_1(\vec{x}_2,\vec{x}_1') & \gamma_1(\vec{x}_2,\vec{x}_2') \end{vmatrix} \tag{7.36}$$

Now we can determine the energy as functional of the density operator and in terms of the one-electron and two-electron operators,

$$E_{HF}[\gamma] = \langle \psi_{ele}^{HF} | \hat{H}_{ele} | \psi_{ele}^{HF} \rangle \tag{7.37}$$

$$= \langle \psi_{ele}^{HF} | \hat{O}_1 | \psi_{ele}^{HF} \rangle + \langle \psi_{ele}^{HF} | \hat{O}_2 | \psi_{ele}^{HF} \rangle \tag{7.38}$$

$$= \int d\vec{x}_1 \hat{O}_1(\vec{x}_1)\gamma(\vec{x}_1,\vec{x}_1')|_{\vec{x}_1=\vec{x}_1'} + \int d\vec{x}_1 d\vec{x}_2 \hat{O}_2(\vec{x}_1',\vec{x}_1,\vec{x}_2',\vec{x}_2)\gamma_2(\vec{x}_1',\vec{x}_1,\vec{x}_2',\vec{x}_2)|_{\vec{x}_1'=\vec{x}_1;\vec{x}_2'=\vec{x}_2} \tag{7.39}$$

where we can express γ_2 from equation (7.35) to obtain,

$$E_{HF}[\gamma] = \int d\vec{x}_1 \left(-\frac{1}{2}\nabla_i^2 + \vartheta(\vec{r})\right)\gamma(\vec{x}_1) + \\ + \int d\vec{x}_1 d\vec{x}_2 \frac{1}{r_{12}}\left(\gamma_1(\vec{x}_1,\vec{x}_1)\gamma_1(\vec{x}_2,\vec{x}_2) - \gamma_1(\vec{x}_2,\vec{x}_1)\gamma_1(\vec{x}_1,\vec{x}_2)\right) \tag{7.40}$$

We are looking for the energy in terms of the electron density, which can be easily

obtained by integrating equation (7.40) on the spin coordinate,

$$E_{HF}[\rho] = \int d\vec{r}_1 \left(-\frac{1}{2}\nabla_i^2 + \vartheta(\vec{r}) \right) \rho(\vec{r}_1) + \int d\vec{r}_1 d\vec{r}_2 \frac{1}{r_{12}} \rho_2(\vec{x}_1, \vec{x}_2) \tag{7.41}$$

However, in equation (7.40), we were able to write γ_2 as a linear combination of different γ_1. We to be able to do the same with the electron density. The proof is simple but extensive and since it has been shown for the density operator, we are going straight to the result. It can be done dividing the spin orbitals in those that have spin up (α) and those that have spin down (β) and integrating over the spin coordinates. That process yields,

$$\rho_2(\vec{r}_1, \vec{r}_2) = \frac{1}{2} \left(\rho_1(\vec{r}_1)\rho_1(\vec{r}_2) - \rho_1^{\alpha\alpha}(\vec{r}_1, \vec{r}_2)\rho_1^{\alpha\alpha}(\vec{r}_2, \vec{r}_1) - \rho_1^{\beta\beta}(\vec{r}_1, \vec{r}_2)\rho_1^{\beta\beta}(\vec{r}_2, \vec{r}_1) \right) \tag{7.42}$$

Ergo, the energy can be written in terms of the electron density, such as,

$$\begin{aligned}
E_{HF}[\rho] = & \int d\vec{r}_1 \left(-\frac{1}{2}\nabla_i^2 + \vartheta(\vec{r}) \right) \rho(\vec{r}_1) + \\
& + \frac{1}{2} \int d\vec{r}_1 d\vec{r}_2 \frac{1}{r_{12}} \left(\rho_1(\vec{r}_1)\rho_1(\vec{r}_2) - \rho_1^{\alpha\alpha}(\vec{r}_1, \vec{r}_2)\rho_1^{\alpha\alpha}(\vec{r}_2, \vec{r}_1) - \rho_1^{\beta\beta}(\vec{r}_1, \vec{r}_2)\rho_1^{\beta\beta}(\vec{r}_2, \vec{r}_1) \right) \\
& = \int d\vec{r}_1 \left(-\frac{1}{2}\nabla_i^2 \right) \rho(\vec{r}_1) + \int d\vec{r}_1 \vartheta(\vec{r})\rho(\vec{r}_1) + \frac{1}{2} \int d\vec{r}_1 d\vec{r}_2 \frac{1}{r_{12}} \rho_1(\vec{r}_1)\rho_1(\vec{r}_2) + \\
& - \frac{1}{2} \int d\vec{r}_1 d\vec{r}_2 \left(\rho_1^{\alpha\alpha}(\vec{r}_1, \vec{r}_2)\rho_1^{\alpha\alpha}(\vec{r}_2, \vec{r}_1) - \rho_1^{\beta\beta}(\vec{r}_1, \vec{r}_2)\rho_1^{\beta\beta}(\vec{r}_2, \vec{r}_1) \right)
\end{aligned}$$

where we define,

$$E_{HF}[\rho] = T[\rho] + V_{ne}[\rho] + \mathscr{J}[\rho] - \mathscr{K}[\rho] \tag{7.43}$$

$$= T[\rho] + V_{ne}[\rho] + V_{ee}[\rho] \tag{7.44}$$

in which $T[\rho]$ is the the electron kinetic energy operator, $V_{ne}[\rho]$ is the interaction operator between electrons and nuclei, $\mathscr{J}[\rho]$ is the Coulomb integral and $\mathscr{K}[\rho]$ is the exchange integral.

To summarize, we have shown that for the Hartree-Fock solution to the electronic problem, we can obtain the first and second order reduced density operators in order to find its corresponding energy. Said energy can be written in terms of only the electron density. These conclusions lay the ground work to demonstrate theorems in Density Functional Theory. The proceedings for DFT's theorems are done in chapter 2.

Functional minimization

Let's take a step back and return to the fundamentals of Classical Mechanics. Consider two points in space (figure 7.1) connected by infinite different trajectories.

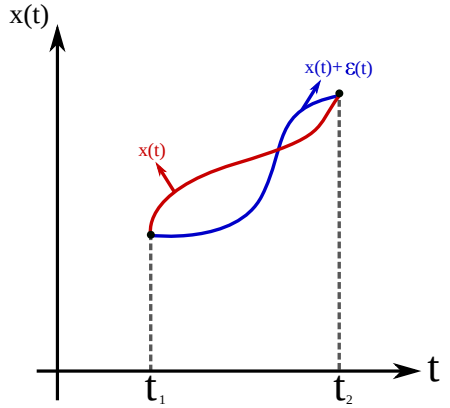

Figure 7.1: Different trajectories between $x(t_1)$ and $x(t_2)$.

The action S is a functional of the Lagrangian $\mathscr{L}$ in the form of

$$S[\mathscr{L}] = \int_{t_1}^{t_2} dt \mathscr{L}(x, \dot{x}, t) \tag{7.45}$$

where

$$\mathscr{L}(x,\dot{x},t) = T - U \tag{7.46}$$

$$= \frac{1}{2}m\dot{x}^2 - U(x). \tag{7.47}$$

When can ask the question of which $x(t)$ minimizes S, or in other words, for which $x(t)$ do we have $dS = 0$. Suppose that $x(t) \to x(t) + \varepsilon(t)$ such that,

$$\frac{dx}{dt} \to \frac{dx}{dt} + \frac{d\varepsilon}{dt} \tag{7.48}$$

with the boundary condition that $\varepsilon(t_1) = \varepsilon(t_2) = 0$. We can write

$$dS = \int_{t_1}^{t_2} dt d\mathscr{L}(x,\dot{x},t) \tag{7.49}$$

in which

$$d\mathscr{L} = \frac{m}{2}\cdot 2\frac{dx}{dt}\frac{d\varepsilon}{dt} - \frac{dU}{dx}\varepsilon(t) \tag{7.50}$$

$$= m\frac{dx}{dt}\frac{d\varepsilon}{dt} - \frac{dU}{dx}\varepsilon(t) \tag{7.51}$$

$$= \frac{d}{dt}\left(m\frac{dx}{dt}\varepsilon\right) - m\frac{d^2x}{dt^2}\varepsilon - \frac{dU}{dx}\varepsilon \tag{7.52}$$

From that, we can insert back into dS,

$$dS = \int_{t_1}^{t_2} dt d\mathscr{L}(x,\dot{x},t) = 0 \tag{7.53}$$

$$= \int_{t_1}^{t_2} dt \left(\frac{d}{dt}\left(m\frac{dx}{dt}\varepsilon \right) - m\frac{d^2x}{dt^2}\varepsilon - \frac{dU}{dx}\varepsilon \right) = 0 \tag{7.54}$$

$$= \int_{t_1}^{t_2} dt \left(m\frac{d^2x}{dt^2} - \frac{dU}{dx} \right) \varepsilon = 0 \tag{7.55}$$

resulting in

$$m\frac{d^2x}{dt^2} - \frac{dU}{dx} = 0 \longrightarrow -\frac{dU}{dx} = F = m\frac{d^2x}{dt^2} \tag{7.56}$$

which is a form of obtaining Newton's Second Law. The idea of minimizing an action comes in handy when working on the core theorems of DFT.

Kohn-Sham equations derivation

From results shown in chapter 2, we know that the electron density with the spin coordinate is

$$\rho(\vec{r}) = \sum_i \chi_i(\vec{x})\chi_i^*(\vec{x}) = \sum_i |\chi_i(\vec{x})|^2 = \sum_i \sum_\omega |\psi^\omega(\vec{r})|^2 \tag{7.57}$$

and the Kohn-Sham energy functional is

$$E_{KS}[\rho] = T_{\mathscr{A}}[\rho] + \int V_{eff}(\vec{r})\rho d\vec{r} \tag{7.58}$$

$$= \sum_i \int d\vec{x}\chi_i^*(\vec{x}) \left(-\frac{1}{2}\nabla^2 \right) \chi_i(\vec{x}) + \sum_i \int d\vec{x} V_{eff}(\vec{r})\chi_i^*(\vec{x})\chi_i(\vec{x}) \tag{7.59}$$

Note that in order for us to write $T_{\mathscr{A}}[\rho]$ the way done above, it's necessary that the wave functions are orthogonal, thus,

$$\int d\vec{x}\psi_i^*(\vec{x})\psi_i(\vec{x}) = \delta_{ij} \tag{7.60}$$

meaning there is no overlap between electron orbitals. Defining the functional $\Omega[\{\psi_i\}]$ to minimize E_{KS} using the electron density restriction we have,

$$\Omega[\{\psi_i\}] = E_{KS}[\rho] - \sum_i \varepsilon_i \left(\int \psi_i^*(\vec{r})\psi_i(\vec{r})d\vec{r} - 1 \right) \tag{7.61}$$

from which we have

$$d\Omega[\{\psi_i\}] = \frac{dE_{KS}[\rho]}{d\psi_k^*} - \sum_i \varepsilon_i \psi_i(\vec{r})\delta_{ik} = 0 \tag{7.62}$$

$$= \frac{dT_{\mathscr{A}}[\rho]}{d\psi_k^*} + \frac{d}{d\psi_k^*} \int V_{eff}(\vec{r})\rho(\vec{r})d\vec{r} - \varepsilon_k \psi_k(\vec{r}) = 0 \tag{7.63}$$

where

$$\frac{dT_{\mathscr{A}}[\rho]}{d\psi_k^*} = \frac{d}{d\psi_k^*} \int \psi_i^*(\vec{r}) \left(-\frac{1}{2}\nabla^2 \right) \psi_i(\vec{r}) \tag{7.64}$$

$$= -\frac{1}{2}\nabla^2 \psi_k \tag{7.65}$$

and

$$\frac{d}{d\psi_k^*}\int V_{eff}(\vec{r})\rho(\vec{r})d\vec{r} = \frac{d}{d\psi_k^*}\sum_i \int V_{eff}(\vec{r})\psi_i^*(\vec{r})\psi_i(\vec{r})d\vec{r} \tag{7.66}$$

$$= V_{eff}(\vec{r})\psi_k(\vec{r}) \tag{7.67}$$

turning equation (7.63) into

$$-\frac{1}{2}\nabla^2\psi_k(\vec{r}) + V_{eff}(\vec{r})\psi_k(\vec{r}) = \varepsilon_k\psi_k(\vec{r}) \tag{7.68}$$

which is the single particle equation for system $\mathscr{A}$ considering $V_{\mathscr{A}} = V_{eff}$.

Note that,

$$\sum_k \varepsilon_k = \sum_k \int d\vec{r}\psi_k^*(\vec{r})\left(-\frac{1}{2}\nabla^2 + V_{eff}(\vec{r})\right)\psi_k(\vec{r}) \tag{7.69}$$

$$= T_{\mathscr{A}}[\rho] + \int V_{eff}(\vec{r})\rho(\vec{r})d\vec{r} \tag{7.70}$$

in which

$$V_{eff}(\vec{r}) = \vartheta(\vec{r}) + \int \frac{\rho(\vec{r}')}{|\vec{r}-\vec{r}'|} + \vartheta_{XC}(\vec{r}) \tag{7.71}$$

where the second term on the right-hand side is known as the Hartree potential and the exchange

and correlation term is $\vartheta_{XC}(\vec{r}) = dE_{XC}[\rho]/d\rho$. It follows that the system's total energy is

$$E[\rho] = T_{\mathscr{A}}[\rho] + \mathscr{J}[\rho] + E_{XC}[\rho] + \int \vartheta(\vec{r})\rho(\vec{r})d\vec{r} \tag{7.72}$$

$$= \sum_k \varepsilon_k - \frac{1}{2}\int d\vec{r}d\vec{r}' \frac{\rho(\vec{r}')\rho(\vec{r})}{|\vec{r}-\vec{r}'|} + E_{XC} - \int d\vec{r}\vartheta_{XC}(\vec{r}). \tag{7.73}$$

Physically, that translates into the sum of orbital energies in Kohn-Sham being different than the total electronic energy.

CHAPTER 8

APPENDIX C

This chapter is divided into two different sections. First, we make an exposè on morphology information for all simulated cases. Next, results from KMC simulations are further detailed.

Methodology

In this section we present further numerical details on the morphology presented in chapter 3. Below, we show the distances between layers present on one side of the box for different nGO concentrations with average intermolecular distances of 75 Å and 145 Å as well as considering different degrees of aggregation, namely q in equation (3.19). It is worth mentioning that those distances are mirrored respective to the central molecule in the center of the box, as shown in figure 3.5. We show the effect that the degree of aggregation has in the intermolecular distance distribution.

d_{dye}(Å)	Layer	Intermolecular distance (Å)		
		$q = 0.80$	$q = 0.85$	$q = 0.90$
75	1	384.7	291.9	205.0
	2	307.8	248.2	184.5
	3	246.2	210.9	166.0
	4	196.9	179.3	149.5
	5	157.6	152.4	134.5
	6	126.1	129.5	121.0
	7	100.9	110.1	108.9
	8	80.7	93.6	98.1
	9	64.5	79.5	88.2
	10	51.6	67.6	79.4
	11	41.3	57.4	71.5
	12	33.1	48.8	64.3
	13	26.4	41.5	57.9
	14	21.1	35.3	52.1
	15	16.9	30.0	46.9
	16	13.5	25.5	42.2
	17	10.8	21.6	37.9
	18	8.6	18.4	34.2
	19	6.9	15.6	30.8
	20	5.5	13.3	27.7
	21	4.4	11.3	24.9
	22	3.5	9.6	22.4
	23	2.8	8.1	20.2
	24	2.2	6.9	18.1
	25	1.8	5.9	16.3
	26	1.5	5.0	14.7

Table 8.1: Intermolecular distances for nGO concentration of 2.96 g/L in the case of AlClPc concentration of 2.26 g/L - equivalent to an average intermolecular distance of $d_1 = 75$ Å - with $L_{box} = 383.6$ nm. Three different levels of aggregation are shown, $q = 0.80$, $q = 0.85$ and $q = 0.90$.

Below we show the same data now considering $\rho_{nGO} = 6.30$ g/L. Noting the number of layers changes due to how we calculated the size of cubic boxes implemented in KMC

simulations.

d_{dye}(Å)	Layer	Intermolecular distance (Å)		
		$q = 0.80$	$q = 0.85$	$q = 0.90$
75	1	301.5	232.5	169.6
	2	241.1	197.6	152.6
	3	192.9	167.9	137.3
	4	154.3	142.7	123.6
	5	123.4	121.3	111.2
	6	98.7	103.1	100.1
	7	79.0	87.6	90.1
	8	63.2	74.5	81.1
	9	50.5	63.3	73.0
	10	40.4	53.8	65.7
	11	32.3	45.7	59.1
	12	25.8	38.9	53.2
	13	20.7	33.0	47.9
	14	16.5	28.1	43.1
	15	13.2	23.8	38.8
	16	10.6	20.3	34.9
	17	8.4	17.2	31.4
	18	6.7	14.6	28.2
	19	5.4	12.4	25.4
	20	4.3	10.6	22.9

Table 8.2: Intermolecular distances for nGO concentration of 6.30 g/L in the case of AlClPc concentration of 2.26 g/L - equivalent to an average intermolecular distance of $d_1 = 75$ Å - with $L_{box} = 298.0$ nm. Three different levels of aggregation are shown, $q = 0.80$, $q = 0.85$ and $q = 0.90$.

d_{dye}(Å)	Layer	Intermolecular distance (Å)		
		$q = 0.80$	$q = 0.85$	$q = 0.90$
75	1	242.8	191.1	144.8
	2	194.2	162.5	130.3
	3	155.4	138.1	117.3
	4	124.3	117.4	105.5
	5	99.4	99.8	95.0
	6	79.5	84.8	85.5
	7	63.6	72.1	76.9
	8	50.9	61.2	69.2
	9	40.7	52.0	62.3
	10	32.5	44.2	56.1
	11	26.0	37.6	50.5
	12	20.8	31.9	45.4
	13	16.6	27.1	40.9
	14	13.3	23.1	36.8
	15	10.6	19.6	33.1
	16	8.5	16.7	29.8

Table 8.3: Intermolecular distances for nGO concentration of 12.65 g/L in the case of AlClPc concentration of 2.26 g/L - equivalent to an average intermolecular distance of $d_1 = 75$ Å - with $L_{box} = 236.0$ nm. Three different levels of aggregation are shown, $q = 0.80$, $q = 0.85$ and $q = 0.90$.

As explained in chapter 4, throughout the experimental work, two different concentrations of photodynamic agent were used. Each rendered a different morphology. The experimental measurement that led to the observation of quenching in emission spectra was performed with only one of the two concentrations, $\rho_{dye} = 0.31$ g/L. Respective intermolecular distances for different aggregation levels are presented below.

n

d_{dye}(Å)	Layer	Intermolecular distance (Å)		
		$q = 0.80$	$q = 0.85$	$q = 0.90$
145	1	486.9	381.0	285.6
	2	389.5	323.8	257.0
	3	311.6	275.3	231.3
	4	249.3	234.0	208.2
	5	199.4	198.9	187.4
	6	159.5	169.0	168.6
	7	127.6	143.7	151.7
	8	102.1	122.1	136.6
	9	81.6	103.8	122.9
	10	65.3	88.2	110.6
	11	52.2	75.0	99.5
	12	41.8	63.7	89.6
	13	33.4	54.2	80.6
	14	26.7	46.0	72.6
	15	21.4	39.1	65.3
	16	17.1	33.2	58.8
	17	13.7	28.2	52.9

Table 8.4: Intermolecular distances for nGO concentration of 2.96 g/L in the case of AlClPc concentration of 0.31 g/L - equivalent to an average intermolecular distance of $d_2 = 145$ Å - with $L_{box} = 476.0$ nm. Three different levels of aggregation are shown, $q = 0.80$, $q = 0.85$ and $q = 0.90$.

These charts represent the numerical values that compiled to distribution plots in figure 3.6 for average intermolecular distance of 75 Å, while figure 3.7 shows the same plots for average intermolecular distance of 145 Å.

d_{dye}(Å)	Layer	Intermolecular distance (Å)		
		$q = 0.80$	$q = 0.85$	$q = 0.90$
145	1	391.9	316.0	248.3
	2	313.5	268.6	223.4
	3	250.8	228.3	201.1
	4	200.6	194.1	181.0
	5	160.5	164.9	162.9
	6	128.4	140.2	146.6
	7	102.7	119.2	131.9
	8	82.1	101.3	118.7
	9	65.7	86.1	106.9
	10	52.6	73.2	96.2
	11	42.0	62.2	86.5
	12	33.6	52.8	77.9
	13	26.9	44.9	70.1

Table 8.5: Intermolecular distances for nGO concentration of 6.30 g/L in the case of AlClPc concentration of 0.31 g/L - equivalent to an average intermolecular distance of $d_2 = 145$ Å - with $L_{box} = 370.4$ nm. Three different levels of aggregation are shown, $q = 0.80$, $q = 0.85$ and $q = 0.90$.

d_{dye}(Å)	Layer	Intermolecular distance (Å)		
		$q = 0.80$	$q = 0.85$	$q = 0.90$
145	1	328.2	273.6	224.9
	2	262.5	232.5	202.4
	3	210.0	197.6	182.1
	4	168.0	168.0	163.9
	5	134.4	142.8	147.5
	6	107.5	121.4	132.8
	7	86.0	103.1	119.5
	8	68.8	87.7	107.5
	9	55.0	74.5	96.8
	10	44.0	63.3	87.1

Table 8.6: Intermolecular distances for nGO concentration of 12.65 g/L in the case of AlClPc concentration of 0.31 g/L - equivalent to an average intermolecular distance of $d_2 = 145$ Å - with $L_{box} = 293.0$ nm. Three different levels of aggregation are shown, $q = 0.80$, $q = 0.85$ and $q = 0.90$.

Results

In this section, we present secondary results from KMC simulations. In the following figures we present TRPL spectra for multiple simulated cases without taking aggregation effects into account.

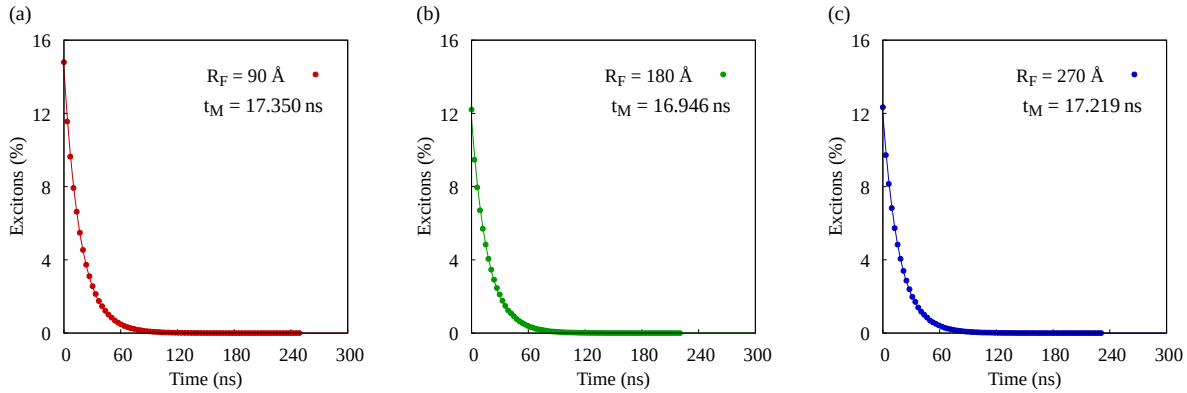

Figure 8.1: AlClPc TRPL spectra in $\rho_{dye} = 2.26$ g/L and $\rho_{nGO} = 2.96$ g/L without aggregation effects. Three different radii between AlClPc and nGO are contemplated.

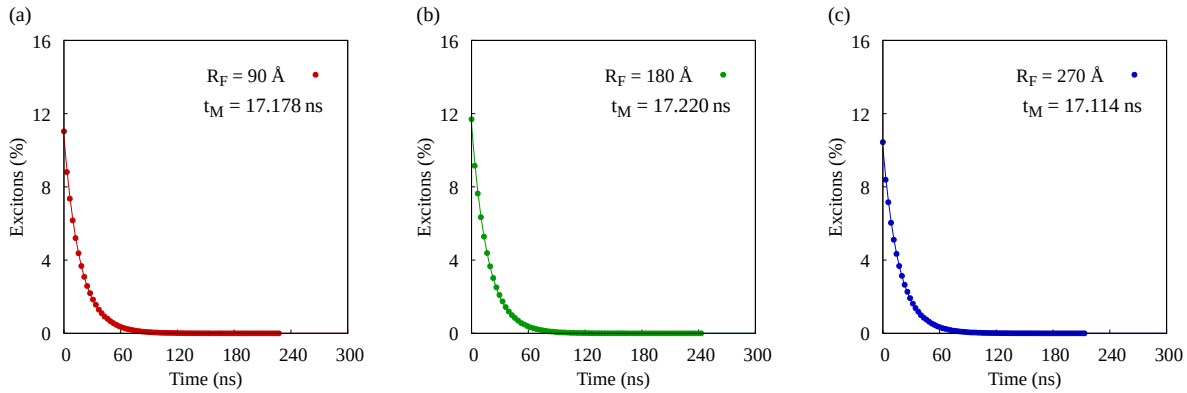

Figure 8.2: AlClPc TRPL spectra in $\rho_{dye} = 2.26$ g/L and $\rho_{nGO} = 6.30$ g/L without aggregation effects. Three different radii between AlClPc and nGO are contemplated.

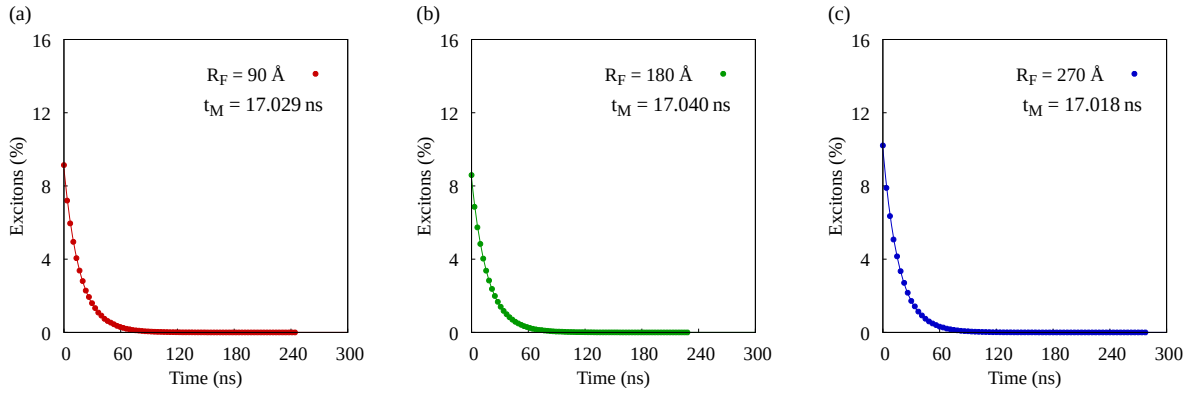

Figure 8.3: AlClPc TRPL spectra in $\rho_{dye} = 2.26$ g/L and $\rho_{nGO} = 12.65$ g/L without aggregation effects. Three different radii between AlClPc and nGO are contemplated.

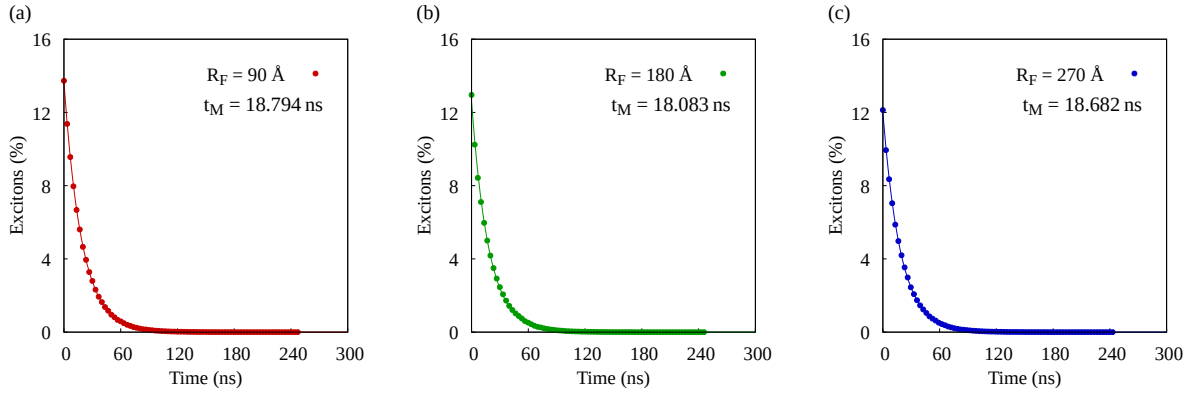

Figure 8.4: AlClPc TRPL spectra in $\rho_{dye} = 0.31$ g/L and $\rho_{nGO} = 2.96$ g/L without aggregation effects. Three different radii between AlClPc and nGO are contemplated.

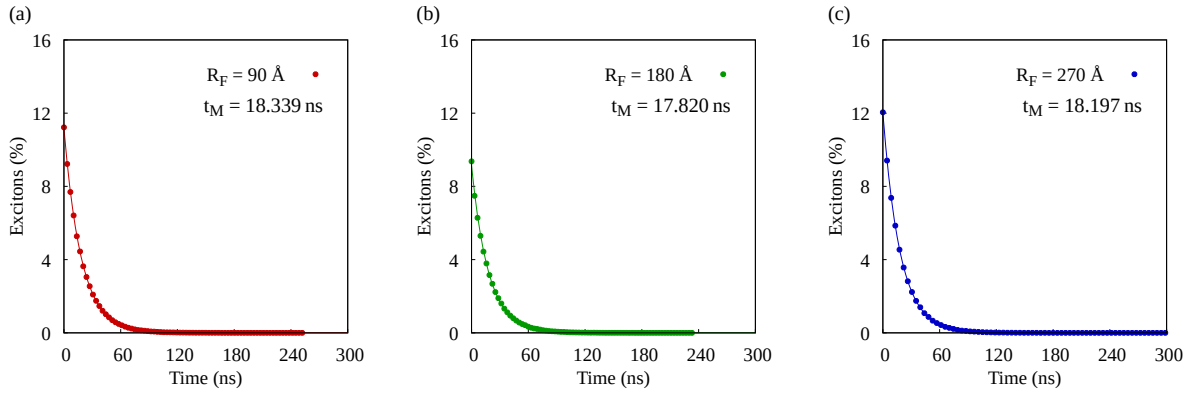

Figure 8.5: AlClPc TRPL spectra in $\rho_{dye} = 0.31$ g/L and $\rho_{nGO} = 6.30$ g/L without aggregation effects. Three different radii between AlClPc and nGO are contemplated.

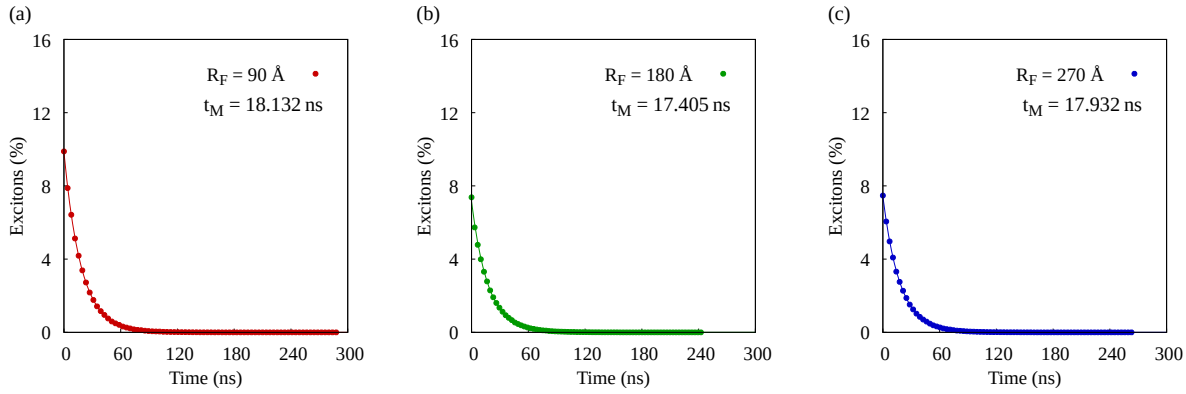

Figure 8.6: AlClPc TRPL spectra in $\rho_{dye} = 0.31$ g/L and $\rho_{nGO} = 12.65$ g/L without aggregation effects. Three different radii between AlClPc and nGO are contemplated.

Bibliography

[1] Elizabeth Ward, Recinda L Sherman, S Jane Henley, Ahmedin Jemal, David A Siegel, Eric J Feuer, Albert U Firth, Betsy A Kohler, Susan Scott, Jiemin Ma, Robert N Anderson, Vicki Benard, and Kathleen Cronin. Annual Report to the Nation on the Status of Cancer, 1999–2015, Featuring Cancer in Men and Women ages 20–49. JNCI: Journal of the National Cancer Institute, 05 2019.

[2] Zheng Huang. A review of progress in clinical photodynamic therapy. Technology in cancer research treatment, 4(3), 283–293., 2005. (Accessed on 05/10/2022).

[3] Reichert KW Cheng J Krouwer HG Ozker K Whelan HT. Schmidt MH, Meyer GA. Evaluation of photodynamic therapy near functional brain tissue in patients with recurrent brain tumors - pubmed. J Neuroonco, 2004. (Accessed on 05/11/2022).

[4] Tsutsui H Ishizumi T Ichinose S Kuroiwa Y. Okunaka T, Kato H. Photodynamic therapy for peripheral lung cancer. Lung Cancer, 2004. (Accessed on 05/11/2022).

[5] H Kato. History of photodynamic therapy–past, present and future. Gan to kagaku ryoho. Cancer & chemotherapy, 23(1):8–15, 1996.

[6] Huang Z. A review of progress in clinical photodynamic therapy. Technology in cancer research treatment, 4(3), 283–293. (Accessed on 05/10/2022).

[7] Jingquan Liu, Liang Cui, and Dusan Losic. Graphene and graphene oxide as new nanocarriers for drug delivery applications, 2013.

[8] Kim D.E. Kim EJ. et al. Lim, J.H. Functional graphene oxide-based nanosheets for photothermal therapy. Macromol. Res. 26, 557–565., 2018. (Accessed on 05/11/2022).

[9] Alzweiri M Ishaqat A ALSalamat HA Bashatwah RM. Bardaweel SK, Gul M. Reactive oxygen species: the dual role in physiological and pathological conditions of the human body. Eurasian J Med. 50(3):193-201, 2018. (Accessed on 05/11/2022).

[10] Zheng Huang. A review of progress in clinical photodynamic therapy. Technology in cancer research & treatment, 4(3):283–293, 2005.

[11] Essraa A Hussein, Moustafa M Zagho, Gheyath K Nasrallah, and Ahmed A Elzatahry. Recent advances in functional nanostructures as cancer photothermal therapy. International journal of nanomedicine, 13:2897, 2018.

[12] Abhishek Sahu, Won Il Choi, Jong Hyun Lee, and Giyoong Tae. Graphene oxide mediated delivery of methylene blue for combined photodynamic and photothermal therapy. Biomaterials, 34(26):6239–6248, 2013.

[13] Mayara Simonelly Costa dos Santos, Ana Luisa Gouvêa, Ludmilla David de Moura, Leonardo Giordano Paterno, Paulo Eduardo Narcizo de Souza, Ana Paula Bastos, Emanuel Adelino Medeiros Damasceno, Fabiane Hiratsuka Veiga-Souza, Ricardo Bentes de Azevedo, and Sônia Nair Báo. Nanographene oxide-methylene blue as phototherapies platform for breast tumor ablation and metastasis prevention in a syngeneic orthotopic murine model. Journal of nanobiotechnology, 16(1):9, 2018.

[14] Alan R Baggio, Mayara SC Santos, Fabiane HV Souza, Rodrigo B Nunes, Paulo

Eduardo N Souza, Sônia N Báo, Antonio Otavio T Patrocinio, Detlef W Bahnemann, Luciano P Silva, Maria José A Sales, et al. Quenching effects of graphene oxides on the fluorescence emission and reactive oxygen species generation of chloroaluminum phthalocyanine. The Journal of Physical Chemistry A, 122(34):6842–6851, 2018.

[15] W Fuss and Karl-Ludwig Kompa. The importance of spectroscopy for infrared multiphoton excitation. Progress in Quantum Electronics, 7(2):117–151, 1981.

[16] Graham Fleming. Chemical applications of ultrafast spectroscopy. 1986.

[17] David J Tannor and Eric J Heller. Polyatomic raman scattering for general harmonic potentials. The Journal of Chemical Physics, 77(1):202–218, 1982.

[18] Taras Petrenko and Frank Neese. Analysis and prediction of absorption band shapes, fluorescence band shapes, resonance raman intensities, and excitation profiles using the time-dependent theory of electronic spectroscopy. The Journal of chemical physics, 127(16):164319, 2007.

[19] Ron Elber and Martin Karplus. Enhanced sampling in molecular dynamics: use of the time-dependent hartree approximation for a simulation of carbon monoxide diffusion through myoglobin. Journal of the American Chemical Society, 112(25):9161–9175, 1990.

[20] Fernando Bernardi, Massimo Olivucci, and Michael A. Robb. Potential energy surface crossings in organic photochemistry, 1996.

[21] Leonardo Evaristo et. al. de Sousa. Modeling the emission spectra of organic molecules: A competition between franck–condon and nuclear ensemble methods. The Journal of Physical Chemistry A, 2018. (Accessed on 05/03/2022).

[22] Javier Cerezo, Francisco J. Avila Ferrer, Giacomo Prampolini, and Fabrizio Santoro. Modeling solvent broadening on the vibronic spectra of a series of coumarin dyes. from implicit to explicit solvent models, 2015.

[23] Roberto Improta, Vincenzo Barone, and Fabrizio Santoro. Ab initio calculations of absorption spectra of large molecules in solution: Coumarin c153. Angewandte Chemie International Edition, 46(3):405–408, 2007.

[24] Mario Barbatti, Adelia JA Aquino, and Hans Lischka. The uv absorption of nucleobases: semi-classical ab initio spectra simulations. Physical Chemistry Chemical Physics, 12(19):4959–4967, 2010.

[25] Rachel Crespo-Otero and Mario Barbatti. Spectrum simulation and decomposition with nuclear ensemble: formal derivation and application to benzene, furan and 2-phenylfuran. Theoretical Chemistry Accounts, 131(6):1237, 2012.

[26] Volkhard May and Oliver Kühn. Charge and energy transfer dynamics in molecular systems. John Wiley & Sons, 2008.

[27] Th. Forster. Zwischenmolekulare energiewanderung und fluoreszenz. Annalen der Physik, 437, 55-75., 1948. (Accessed on 05/3/2022).

[28] Anna Köhler and Heinz Bässler. Electronic processes in organic semiconductors: An introduction. John Wiley & Sons, 2015.

[29] Aurora Munoz-Losa, Carles Curutchet, Brent P Krueger, Lydia R Hartsell, and Benedetta Mennucci. Fretting about fret: failure of the ideal dipole approximation. Biophysical journal, 96(12):4779–4788, 2009.

[30] Kim F Wong, Biman Bagchi, and Peter J Rossky. Distance and orientation dependence of excitation transfer rates in conjugated systems: beyond the förster theory. The Journal of Physical Chemistry A, 108(27):5752–5763, 2004.

[31] Leonardo Sousa, Fernando Teixeira Bueno, Geraldo Magela e Silva, DEMETRIO A DA SILVA FILHO, and Pedro Henrique Neto. Fast predictions of exciton diffusion length in organic materials. Journal of Materials Chemistry C, 2019.

[32] Shane R Yost, Eric Hontz, Sina Yeganeh, and Troy Van Voorhis. Triplet vs singlet energy transfer in organic semiconductors: the tortoise and the hare. The Journal of Physical Chemistry C, 116(33):17369–17377, 2012.

[33] David L Dexter. A theory of sensitized luminescence in solids. The Journal of Chemical Physics, 21(5):836–850, 1953.

[34] G Vaubel and H Baessler. Diffusion of singlet excitons in tetracene crystals. Molecular crystals and liquid crystals, 12(1):47–56, 1970.

[35] Yasunari Tamai, Yuu Matsuura, Hideo Ohkita, Hiroaki Benten, and Shinzaburo Ito. One-

dimensional singlet exciton diffusion in poly (3-hexylthiophene) crystalline domains. The journal of physical chemistry letters, 5(2):399–403, 2014.

[36] Monishka Rita Narayan and Jai Singh. Roles of binding energy and diffusion length of singlet and triplet excitons in organic heterojunction solar cells. physica status solidi (c), 9(12):2386–2389, 2012.

[37] Pedro Henrique de Oliveira Neto, Demetrio A da Silva Filho, Wiliam F da Cunha, Paulo H Acioli, and Geraldo Magela e Silva. Limit of exciton diffusion in highly ordered π-conjugated systems. The Journal of Physical Chemistry C, 119(34):19654–19659, 2015.

[38] Gleb M Akselrod, Parag B Deotare, Nicholas J Thompson, Jiye Lee, William A Tisdale, Marc A Baldo, Vinod M Menon, and Vladimir Bulović. Visualization of exciton transport in ordered and disordered molecular solids. Nature communications, 5:3646, 2014.

[39] Lekshmi Sudha Devi, Mohammad K Al-Suti, Carsten Dosche, Muhammad S Khan, Richard H Friend, and Anna Köhler. Triplet energy transfer in conjugated polymers. i. experimental investigation of a weakly disordered compound. Physical Review B, 78(4):045210, 2008.

[40] Gaussian 16 | gaussian.com. https://gaussian.com/gaussian16/. (Accessed on 05/16/2022).

[41] Leonardo Evaristo de Sousa, Fernando Teixeira Bueno, Demétrio Antônio da Silva Filho, Luiz Antônio Ribeiro Junior, and Pedro Henrique de Oliveira Neto. Dynamical exciton

decay in organic materials: the role of bimolecular recombination. Physical Chemistry Chemical Physics, 21(4):1711–1716, 2019.

[42] Karsten Reuter. First-principles kinetic monte carlo simulations for heterogeneous catalysis: Concepts, status, and frontiers. ChemInform, 43(36):no, 2012.

[43] Leonardo Evaristo de Sousa, Pedro Henrique de Oliveira Neto, and Demetrio Antônio da Silva Filho. Kinetic monte carlo model for the covid-19 epidemic: Impact of mobility restriction on a covid-19 outbreak, Sep 2020.

[44] Leonardo Evaristo de Sousa, Demétrio Antônio da Silva Filho, Piotr de Silva, Luciano Ribeiro, and Pedro Henrique de Oliveira Neto. A genetic algorithm approach to design principles for organic photovoltaic materials, 2020.

[45] Leonardo Evaristo de Sousa, Pedro Henrique de Oliveira Neto, Jakob Kjelstrup-Hansen, and Demétrio Antônio da Silva Filho. Modeling temperature dependent singlet exciton dynamics in multilayered organic nanofibers, 2018.

[46] Leonardo Evaristo de Sousa, Fernando Teixeira Bueno, Luciano Ribeiro, Luiz Antônio Ribeiro Junior, Demétrio Antônio da Silva Filho, and Pedro Henrique de Oliveira Neto. Role of exciton density in organic materials: Diffusion length, lifetime, and quantum efficiency, 2019.

[47] Robert M. Clegg. Chapter 1 förster resonance energy transfer—fret what is it, why do it, and how it's done. In Fret and Flim Techniques, volume 33 of Laboratory Techniques in Biochemistry and Molecular Biology, pages 1–57. Elsevier, 2009.

[48] Preparation and aggregate state regulation of co-assembly graphene oxide-porphyrin composite langmuir films via surface-modified graphene oxide sheets. colloids and surfaces a: Physicochemical and engineering aspects, 584, 124023 | 10.1016/j.colsurfa.2019.124023.